International Journal for Numerical Methods in Engineering

WILEY

RESEARCH ARTICLE OPEN ACCESS

Surface and Boundary Corrections in Peridynamics Using Optimized Nodal Influence Weights

Arman Shojaei[1] | Greta Ongaro[2] | Alexander Hermann[3] | Stewart A. Silling[4] | Patrizia Trovalusci[2] | Christian J. Cyron[1,3]

[1]Institute of Material Systems Modeling, Helmholtz-Zentrum Hereon, Geesthacht, Germany | [2]Department of Structural and Geotechnical Engineering, Sapienza University of Rome, Rome, Italy | [3]Institute for Continuum and Material Mechanics, Hamburg University of Technology, Hamburg, Germany | [4]Nearforce LLC, Albuquerque, New Mexico, USA

Correspondence: Arman Shojaei (arman.shojaei@hereon.de) | Greta Ongaro (greta.ongaro@uniroma1.it)

Received: 4 February 2026 | **Revised:** 2 June 2026 | **Accepted:** 29 June 2026

Keywords: horizon truncation | nodal influence weights | open-source software | peridynamics | surface correction

ABSTRACT

Peridynamics (PD), similarly to some other nonlocal continuum theories, exhibits truncated interaction horizons near free surfaces, cracks, and voids in bounded domains. This loss of neighbors causes artificial surface effects and inconsistencies in the derivative and energy operators that persist under discretization refinement, limiting PD accuracy and robustness. First, the analysis and numerical isolation of the effects of horizon truncation on these operators are carried out, showing how it induces surface softening in bond-based and stiffening/softening in state-based PD formulations. Then, a purely PD-based surface correction is proposed to restore full-horizon behavior while preserving the original horizon radius and bond topology. Each node is assigned a scalar influence weight, and every bond is scaled by the average of the endpoint weights to maintain symmetry. The nodal influence weights are computed in a preprocessing optimization step enforcing agreement between truncated- and full-horizon derivative and energy operators. Unlike existing approaches, the proposed method does not rely on ghost particles, variable horizons, or reference solutions from classical continuum mechanics (CCM). Benchmarks in one, two, and three dimensions, including a dynamic brittle fracture test, show that the optimized nodal influence weights reduce boundary-induced surface effects, improve energy consistency, and accelerate convergence of PD solutions. Analytical evaluation of the calibration targets over full-horizons also improves interior volume integration accuracy. The proposed scheme is simple to implement in existing PD codes, incurs only a modest preprocessing cost, performs robustly for flat and curved boundaries on both regular and irregular point sets, produces reliable crack paths, and applies to both bond-based and ordinary state-based PD formulations. An open-source Python implementation, `perifit`, is provided.

1 | Introduction

In the last two decades, computational methods based on peridynamic (PD) theory, a nonlocal reformulation of classical continuum mechanics (CCM) based on integro-differential equations, have been widely developed to overcome limitations of local continuum models in the presence of evolving discontinuities. In contrast to CCM, whose strong-form governing equations rely on spatial derivatives of the displacement field, PD describes the motion of a material point through integral interactions with other points located within a finite neighborhood, called *horizon*. The original bond-based (BB) formulation introduced in [1] represents these interactions through pairwise central-force bonds, while the later state-based (SB) formulation [2, 3] generalizes this concept by allowing the force transmitted through a bond to depend on the collective deformation state of the whole family of a material point. The horizon therefore defines the range of nonlocal interactions and introduces an intrinsic material length scale into the model [4].

Since PD is formulated through integral equations rather than spatial differentiation, its governing equations remain meaningful in the presence of discontinuous displacement fields. This feature makes PD particularly attractive for modeling crack nucleation, propagation, branching, coalescence, and fragmentation without special enrichment functions, remeshing strategies, or additional crack-growth criteria [1, 5, 6]. BB-PD remains attractive because of its conceptual simplicity, direct physical interpretation, and computational efficiency, especially for brittle fracture problems. However, the classical central-force BB formulation imposes restrictions on the admissible Poisson's ratio [1]. This limitation has motivated several pure-PD extensions of BB theory, including formulations enriched with bond-rotation effects [7], conjugated bond-pair interactions [8], micropolar or shear-deformable BB models [9], and generalized BB formulations with tension–rotation–shear coupling [10]. These developments preserve, to different degrees, the simplicity of BB interactions while broadening the admissible elastic response and improving the description of shear deformation, mixed-mode fracture, crack initiation, propagation, and coalescence in brittle and quasi-brittle materials [11]. SB-PD provides another generalization by allowing the force transmitted through a bond to depend on the collective deformation state of the whole family of a material point, thereby removing the classical Poisson's ratio restriction and enabling a broader class of constitutive models, including ordinary state-based (OSB) formulations such as the linear peridynamic solid [2, 3]. Accordingly, PD has been applied to impact [12, 13], dynamic fracture [14–19], fatigue [20], thermal and diffusion-type problems [21–26], heterogeneous materials [27–32], and multiphysics systems [33–38].

Despite these advantages, the nonlocal character of PD also introduces difficulties that are absent, or less pronounced, in local continuum models. One difficulty is the increased computational cost associated with neighborhood interactions [39, 40]. Another is the treatment of boundary conditions. In CCM, Dirichlet- and Neumann-type conditions are imposed directly on boundary surfaces. In PD, however, boundaries are nonlocal objects: displacement and traction data must be prescribed over volumetric layers whose thickness is related to the horizon [1, 12, 41–44]. If boundary data are imposed only on the geometric surface, spurious oscillations and boundary artifacts may occur, while the proper volumetric distribution of displacement or traction data is not unique [45, 46].

A second, and more fundamental, difficulty is the so-called surface effect caused by horizon truncation. Material points located near free surfaces, external boundaries, cracks, voids, or pores do not possess full neighborhoods. Their horizons are cut by the boundary, and the symmetry of the full interaction domain is lost. As a consequence, the discrete PD operators near such regions no longer reproduce the behavior for which the bulk constitutive parameters were calibrated. In BB-PD, this defect is commonly observed as artificial surface softening and underestimation of strain energy density [47–50]. In SB formulations, the same loss of horizon symmetry affects family-level operator evaluations and may produce more complex stiffening, softening, or oscillatory errors [45]. Thus, surface effect is not merely a BB stiffness artifact, but a broader operator-consistency problem in nonlocal discretizations with truncated horizons.

This distinction is important because the practical consequences of horizon truncation extend beyond a local stiffness error. Boundary-induced operator inconsistencies can degrade convergence, distort stress and energy fields, alter wave propagation near boundaries, and influence crack initiation and propagation paths. These errors are particularly relevant in surface-dominated systems, such as thin structures, porous materials, films, and problems involving wear, indentation, or evolving fracture surfaces [23, 50–52]. In dynamic fracture simulations, uncorrected surface effects may produce artificial boundary-driven cracks or suppress physically expected crack paths, especially when the horizon-to-grid ratio is moderate and the spatial resolution is not sufficiently fine [16, 50, 52].

Several correction strategies have been proposed to mitigate surface effects in PD. Geometric extension methods introduce fictitious or ghost nodes outside the physical domain in order to complete truncated neighborhoods through mirroring, extrapolation, or optimized boundary layers [44, 46, 53]. These approaches can achieve high accuracy for smooth fields, but they increase the number of degrees of freedom, may introduce artificial energy layers, and are difficult to apply in problems with evolving cracks or complex moving boundaries. Volume correction and force normalization methods rescale nodal volumes, bond stiffnesses, or pairwise forces near boundaries to compensate for missing interactions [41].

Although attractive because of their simplicity, such corrections can be grid-sensitive, may depend on the loading mode, and generally do not enforce systematic consistency of both derivative and energy operators [45].

Energy-based approaches represent a more physically motivated class of corrections. Point-specific schemes fit correction factors by matching local PD energy densities to reference solutions, often obtained from auxiliary homogeneous deformation tests [51]. Analytical bond-specific methods assign direction-dependent factors to individual bonds so that the PD strain energy agrees with the corresponding local continuum energy under affine deformation [50]. While these methods improve energy consistency, they often rely either on CCM reference quantities, local strain information, or geometry-dependent ray–surface distance calculations, which can become costly in large-scale three-dimensional (3D) simulations with complex boundaries. Variable-horizon and adaptive methods reduce or modify the horizon near boundaries [54–57], but this changes the intrinsic nonlocal length scale and may affect dispersion, fracture energy, and the physical interpretation of the model. Finally, CCM–PD coupling methods employ local continuum models away from fracture zones and PD only where discontinuities are expected [40, 58–62]. Such approaches can reduce cost and avoid some boundary difficulties, but they introduce coupling interfaces and related artifacts, and are not purely PD-based.

Despite these advances, PD still lacks a robust, generalizable, and purely nonlocal correction strategy that treats horizon truncation as an operator-consistency problem. Many existing approaches depend on external CCM reference solutions or specific load cases, introduce additional degrees of freedom or iterative procedures, alter the horizon and hence the nonlocal length scale, or compromise symmetry and reciprocity in the global stiffness matrix. Moreover, several corrections are designed primarily for BB formulations and do not directly address the different but related inconsistencies that arise in SB-PD. A correction strategy suitable for both settings should preserve the original PD formulation, remain independent of loading and material response, improve the consistency of the discrete nonlocal operators, and be portable to existing PD solvers.

The present work addresses this gap by introducing a purely PD-based correction strategy based on optimized nodal influence weights. Each node is assigned a scalar weight w_i, and each bond contribution is scaled symmetrically by the factor $(w_j + w_i)/2$. This construction preserves pairwise reciprocity and the symmetry of the global stiffness matrix, while leaving the horizon radius, family topology, and constitutive model unchanged. The weights are computed once in a geometry-dependent and load-independent preprocessing step. For a finite set of polynomial test functions, agreement is enforced between discrete truncated-horizon PD derivative and energy operators and their analytical full-horizon counterparts. The calibration therefore uses PD-to-PD matching: the truncated operator is corrected toward the corresponding full-horizon PD operator without invoking CCM reference solutions, fictitious nodes, or auxiliary simulations.

A central contribution of the paper is that the same correction philosophy is developed consistently for both BB-PD and OSB-PD. In both cases, the method is formulated through the matching of derivative and energy operators rather than through a problem-specific stiffness factor or a direct modification of individual constitutive quantities. A modal analysis is performed, showing that horizon truncation activates odd horizon moments that vanish in the full-horizon setting. This loss of parity explains the systematic softening observed in BB-PD and the more complex stiffening/softening behavior observed in OSB-PD. Although these effects manifest differently in the two formulations, they originate from the same algebraic source: the loss of symmetry of the nonlocal integration domain. The proposed optimization therefore targets the common operator-level origin of the error.

The significance of the method is broader than a conventional boundary correction. First, it provides a purely PD-based correction that restores full-horizon operator behavior without modifying the constitutive law, changing the horizon size, adding fictitious or ghost nodes, or coupling the model to CCM. The original PD formulation is kept intact, which makes the method highly portable and straightforward to integrate into existing PD solvers. Second, the same optimized nodal influence weights act simultaneously on several sources of numerical inconsistency: they mitigate surface- and boundary-induced errors, improve the accuracy of volume integration also in the interior of the domain, and regularize the convergence behavior under spatial refinement. Thus, the correction is not limited to boundary nodes, but consistently improves the discrete nonlocal operators throughout the computational domain. Third, the symmetric bond scaling preserves pairwise reciprocity and global stiffness symmetry, which are essential for stable and physically consistent discrete systems. Finally, the computation of the weights requires only a one-time preprocessing step. The resulting system is sparse and well conditioned, can be solved efficiently with standard iterative solvers, and adds only a modest computational overhead compared with the subsequent PD simulation.

Numerical examples in one, two, and three dimensions demonstrate the performance of the proposed formulation, referred to as the *modified-PD* approach, on regular and irregular point sets, flat and curved boundaries, and dynamic fracture problems. The optimized nodal influence weights reduce boundary-induced artifacts, improve energy consistency, produce more regular convergence trends under spatial refinement, and suppress spurious boundary-driven crack initiation while preserving physically meaningful crack paths. Since, the analytical full-horizon targets are evaluated independently of the applied loading, the same weights can be reused for different boundary-value problems on the same point set and horizon. A ready-to-use implementation of the weight-computation procedure is provided in the open-source Python package `perifit`[63].

The remainder of this paper is organized as follows. Section 2 reviews the BB-PD and OSB-PD formulations used in this work, together with the adopted meshfree discretization and boundary conditions treatment. Section 3 analyzes the origin of horizon-truncation errors through full-horizon and truncated-horizon modal operators. Section 4 introduces the optimized nodal influence weight correction and its application to BB-PD and OSB-PD through derivative- and energy-operator matching. Section 5 presents numerical examples assessing accuracy, convergence, robustness, and fracture behavior of the proposed formulation. Section 6 concludes the paper by summarizing the main findings.

2 | Overview of Peridynamics

Consider a body occupying a domain $\Omega \subset \mathbb{R}^d$ with d the spatial dimension. In PD, each material point $\mathbf{x} \in \Omega$ interacts directly only with other material points located within a finite *neighborhood*, $\mathcal{H}_{\mathbf{x}} := \{\mathbf{x}' \in \Omega \ : \ \|\mathbf{x}' - \mathbf{x}\| \le \delta\}$, where δ is the PD *horizon* (see Figure 1). The reference bond vector is $\boldsymbol{\xi} := \mathbf{x}' - \mathbf{x}$, while the relative displacement vector is $\boldsymbol{\eta} := \mathbf{u}(\mathbf{x}', t) - \mathbf{u}(\mathbf{x}, t)$, so that $\boldsymbol{\eta} + \boldsymbol{\xi}$ represents the deformed bond.

In its most general SB form [2], the PD equation of motion reads:

$$\rho(\mathbf{x})\, \ddot{\mathbf{u}}(\mathbf{x}, t) = \int_{\mathcal{H}_{\mathbf{x}}} \left\{ \underline{\mathbf{T}}[\mathbf{x}, t]\langle \xi \rangle - \underline{\mathbf{T}}[\mathbf{x}', t]\langle -\xi \rangle \right\} \, \mathrm{d}V_{\mathbf{x}'} + \mathbf{b}(\mathbf{x}, t), \tag{1}$$

where ρ is the mass density, $\ddot{\mathbf{u}}$ is the acceleration, $\underline{\mathbf{T}}[\mathbf{x}, t]\langle \xi \rangle$ is the *force vector state* that $\mathbf{x}$ exerts through the bond $\boldsymbol{\xi}$, and $\mathbf{b}$ is a prescribed body force density field. In PD, the scalar-valued *influence function* $\omega(\|\xi\|)$ is introduced to modulate the bond strength within the horizon [64, 65]. Two common forms are (see Figure 2):

$$\omega(\|\xi\|) := \begin{cases} 1 & (\text{constant}, \ \omega_0), \\ 1 - \dfrac{\|\xi\|}{\delta} & (\text{conical}, \ \omega_1), \end{cases} \quad \text{for } \|\xi\| \le \delta, \qquad \omega(\|\xi\|) := 0, \ \text{for } \|\xi\| > \delta. \tag{2}$$

Unless otherwise stated, the constant influence function $\omega = \omega_0$ is adopted throughout this work. Specific constitutive models are obtained by specializing $\underline{\mathbf{T}}$; two such models, BB and OSB PD, are summarized below.

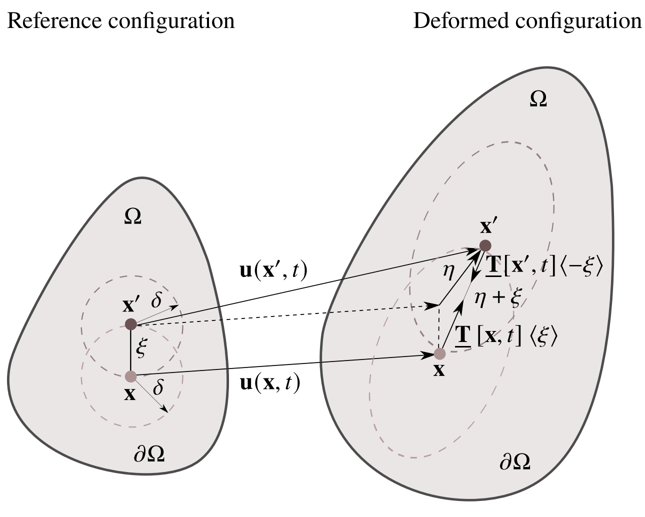

FIGURE 1 | Representation of a generic PD domain Ω before and after deformation.

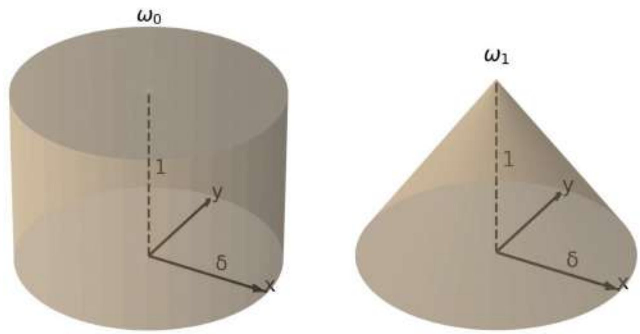

FIGURE 2 | Constant (left) and conical (right) influence functions ω.

2.1 | BB Peridynamics

In the BB formulation [1], interactions are strictly pairwise: the force depends only on the individual bond connecting the two material points. The *prototype microelastic brittle* (PMB) material model [12, 65] defines the pairwise force function

$$\mathbf{f}(\boldsymbol{\eta}, \xi) = \omega(\|\xi\|)\; c\; s\; \frac{\boldsymbol{\eta}+\xi}{\|\boldsymbol{\eta}+\xi\|}, \tag{3}$$

where $s = (\|\boldsymbol{\eta}+\xi\| - \|\xi\|)/\|\xi\|$ is the bond stretch and c is the *micromodulus* constant. In the SB framework, the BB force vector state is $\underline{\mathbf{T}}^{\mathrm{BB}}\langle\xi\rangle = \mathbf{f}/2$, and the equation of motion (1) reduces to $\rho\ddot{\mathbf{u}} = \int_{\mathcal{H}_{\mathbf{x}}} \mathbf{f}\, \mathrm{d}V_{\mathbf{x}'} + \mathbf{b}$.

Because BB-PD relies on central-force interactions, the Poisson's ratio is fixed to $\nu = 1/4$ in 3D and 2D plane strain problems, and $\nu = 1/3$ in plane stress conditions [1]. Matching PD strain energy with classical linear elasticity under homogeneous deformation yields [12, 66, 67]:

$$c = \begin{cases} \dfrac{18K}{\pi\delta^4} & & \text{3D}(\omega = \omega_0), \\[2mm] \dfrac{9E}{\pi\delta^3}(\omega = \omega_0), & \dfrac{36E}{\pi\delta^3}(\omega = \omega_1) & \text{plane stress}, \\[2mm] \dfrac{48E}{5\pi\delta^3}(\omega = \omega_0), & \dfrac{192E}{5\pi\delta^3}(\omega = \omega_1) & \text{plane strain}, \end{cases} \tag{4}$$

where K is the bulk modulus and E is the Young's modulus.

In the small-deformation regime ($\|\boldsymbol{\eta}\| \ll \delta$), the stretch linearizes to $s \approx \xi \cdot \boldsymbol{\eta}/\|\xi\|^2$ and the bond direction reduces to $\xi/\|\xi\|$. The resulting linearized BB (LBB) force vector state and strain energy density are [1, 68]:

$$\underline{\mathbf{T}}^{\mathrm{LBB}}[\mathbf{x}]\langle\xi\rangle = \frac{1}{2}\omega(\|\xi\|)c\frac{\xi\otimes\xi}{\|\xi\|^3}\boldsymbol{\eta}, \tag{5}$$

$$W^{\mathrm{LBB}}(\mathbf{x}) = \frac{c}{4}\int_{\mathcal{H}_{\mathbf{x}}} \omega(\|\xi\|)\frac{(\xi\cdot\boldsymbol{\eta})^2}{\|\xi\|^3}\mathrm{d}V_{\mathbf{x}'}. \tag{6}$$

2.2 | OSB Peridynamics

In the OSB formulation [2], the force vector state remains parallel to the deformed bond but its magnitude depends on the collective deformation of the entire family, thereby removing the Poisson's ratio restriction. The *weighted volume* at $\mathbf{x}$ is defined as:

$$\tilde{m}(\mathbf{x}) := \int_{\mathcal{H}_{\mathbf{x}}} \omega(\|\xi\|)\|\xi\|^2 \mathrm{d}V_{\mathbf{x}'}, \tag{7}$$

the nonlocal *dilatation* as:

$$\overline{\theta}(\mathbf{x}, t) := \frac{d}{\tilde{m}(\mathbf{x})}\int_{\mathcal{H}_{\mathbf{x}}} \omega(\|\xi\|)e(\xi, t)\|\xi\|\mathrm{d}V_{\mathbf{x}'}, \tag{8}$$

where d is the spatial dimension and $e(\xi, t) := \|\eta + \xi\| - \|\xi\|$ is the bond *extension*, and the *deviatoric extension* as:

$$e^{\mathrm{d}}(\xi, t) := e(\xi, t) - \frac{\overline{\theta}\|\xi\|}{d}. \tag{9}$$

The strain energy density takes the form [2, 3]:

$$W^{\mathrm{OSB}}(\mathbf{x}) = a\overline{\theta}^2 + b\int_{\mathcal{H}_{\mathbf{x}}} \omega(\|\xi\|)\left(e^{\mathrm{d}}\right)^2 \mathrm{d}V_{\mathbf{x}'}, \tag{10}$$

where a and b are constitutive parameters determined by energy matching with classical elasticity [2, 45]. The force scalar state and force vector state are:

$$\underline{t}[\mathbf{x}, t]\langle\xi\rangle = \frac{2a\ d}{\tilde{m}(\mathbf{x})}\ \omega(\|\xi\|)\ \|\xi\|\ \overline{\theta} + 2b\ \omega(\|\xi\|)\ e^{\mathrm{d}}, \tag{11}$$

$$\underline{\mathbf{T}}^{\mathrm{OSB}}[\mathbf{x}, t]\langle\xi\rangle = \underline{t}\langle\xi\rangle\ \frac{\eta + \xi}{\|\eta + \xi\|}. \tag{12}$$

For three dimensions ($d = 3$), the calibration yields [2, 45]:

$$a = \frac{K}{2}, \qquad b = \frac{15G}{2\ \tilde{m}}, \tag{13}$$

where G is the shear modulus. For a full horizon with ω_0, the analytical weighted volume is $\tilde{m} = 4\pi\delta^5/5$; two-dimensional (2D) counterparts follow with adapted parameters [2, 45].

In the small-deformation regime, the bond extension linearizes to $e \approx \xi \cdot \eta/\|\xi\|$ and the bond direction reduces to $\xi/\|\xi\|$. The resulting *linear peridynamic solid* (LPS) force vector state and strain energy density in 3D read [3]:

$$\underline{\mathbf{T}}^{\mathrm{LPS}}[\mathbf{x}, t]\langle\xi\rangle = \frac{3K - 5G}{\tilde{m}(\mathbf{x})}\ \omega(\|\xi\|)\ \overline{\theta}\ \xi + \frac{15G}{\tilde{m}(\mathbf{x})}\ \omega(\|\xi\|)\ \frac{\xi \otimes \xi}{\|\xi\|^2}\ \eta, \tag{14}$$

$$W^{\mathrm{LPS}}(\mathbf{x}) = \frac{3K - 5G}{6}\ \overline{\theta}^2 + \frac{15G}{2\ \tilde{m}(\mathbf{x})}\int_{\mathcal{H}_{\mathbf{x}}} \omega(\|\xi\|)\ \frac{(\xi \cdot \eta)^2}{\|\xi\|^2}\ \mathrm{d}V_{\mathbf{x}'}, \tag{15}$$

with the linearized dilatation $\overline{\theta} = (3/\tilde{m})\int_{\mathcal{H}_{\mathbf{x}}} \omega(\|\xi\|)\ \xi \cdot \eta\ \mathrm{d}V_{\mathbf{x}'}$.

2.3 | BB Fracture Model

In PD, fracture is incorporated by introducing a history-dependent bond-breakage function $\mu(\xi, t)$ into the constitutive force law. For the PMB material model, this gives:

$$\mathbf{f}(\eta, \xi, t) = \mu(\xi, t)\ \omega(\|\xi\|)\ c\ s\ \frac{\eta + \xi}{\|\eta + \xi\|}, \tag{16}$$

where

$$\mu(\xi, t) = \begin{cases} 1 & \text{if } s(t') < s_0\ \forall\ \ 0 < t' < t, \\ 0 & \text{otherwise.} \end{cases} \tag{17}$$

Once the bond stretch exceeds the *critical stretch* s_0, the bond breaks irreversibly [12]. The critical stretch is related to the critical energy release rate G_0 by [12]:

$$s_0 = \begin{cases} \sqrt{\dfrac{5G_0}{6E\delta}} & & \text{3D } (\omega = \omega_0), \\ \sqrt{\dfrac{4\pi G_0}{9E\delta}}(\omega = \omega_0), & \sqrt{\dfrac{5\pi G_0}{9E\delta}}(\omega = \omega_1) & \text{plane stress,} \\ \sqrt{\dfrac{5\pi G_0}{12E\delta}}(\omega = \omega_0), & \sqrt{\dfrac{25\pi G_0}{48E\delta}}(\omega = \omega_1) & \text{plane strain.} \end{cases} \tag{18}$$

The local damage is quantified by:

$$\varphi(\mathbf{x}, t) := 1 - \frac{\int_{\mathcal{H}_{\mathbf{x}}} \mu(\boldsymbol{\xi}, t)\, \mathrm{d}V_{\mathbf{x}'}}{\int_{\mathcal{H}_{\mathbf{x}}} \mathrm{d}V_{\mathbf{x}'}}, \tag{19}$$

where $\varphi = 0$ represents the undamaged state of the material, while $\varphi = 1$ indicates the complete disconnection of material point $\mathbf{x}$ from its initial neighbors [12].

2.4 | Boundary Conditions

Since the variational formulation of the PD equation of motion does not yield natural (Neumann/traction) boundary conditions, the treatment of boundary conditions in PD differs fundamentally from that in CCM [1, 41]. Surface tractions are represented as equivalent body forces $\mathbf{b}$ in (1), applied within a volumetric layer of thickness at least δ beneath the corresponding surface; displacement (Dirichlet) conditions are likewise prescribed within a layer of thickness at least δ [41].

2.5 | Meshfree Discretization

The most widely adopted discretization, which is also employed here, is the meshfree scheme [12], commonly referred to as *standard* scheme [52, 69]. The domain is partitioned into N nodes $\mathbf{x}_i$, $i = 1, \dots, N$, each carrying a volume V_i. For a uniform grid with spacing Δx, the nodal volume is $V_i = (\Delta x)^d$. No elements or other geometric links are introduced [12]. The *family* of node $\mathbf{x}_i$ is defined as $\mathcal{F}_i := \{j : 0 < \|\mathbf{x}_j - \mathbf{x}_i\| \le \delta\}$.

With time discretized into instants $t^0, t^1, \dots, t^n$ at constant step Δt, one-point quadrature over each family node yields the semi-discrete equation of motion

$$\rho_i\, \ddot{\mathbf{u}}_i^n = \sum_{j \in \mathcal{F}_i} \Big[\underline{\mathbf{T}}_i^n \langle \xi_j \rangle - \underline{\mathbf{T}}_j^n \langle -\xi_j \rangle \Big]\, \beta(\xi_j)\, V_j + \mathbf{b}_i^n, \tag{20}$$

where $\xi_j := \mathbf{x}_j - \mathbf{x}_i$ and $\beta(\xi)$ is a volume correction factor for partial cell–horizon intersection, suggested in [70] for 2D cases, as:

$$\beta(\xi) = \begin{cases} 1 & \|\xi\| \le \delta - \dfrac{\Delta x}{2}, \\ \dfrac{\delta - \|\xi\|}{\Delta x} + \dfrac{1}{2} & \delta - \dfrac{\Delta x}{2} < \|\xi\| < \delta + \dfrac{\Delta x}{2}, \\ 0 & \|\xi\| \ge \delta + \dfrac{\Delta x}{2}. \end{cases} \tag{21}$$

As discussed in Section 4, the surface correction proposed in this work does not rely on $\beta(\xi)$; the optimized nodal influence weights play an analogous corrective role.

Time integration is performed by exploiting the velocity-Verlet algorithm [12]. For numerical stability, the time step must satisfy [12]

$$\Delta t < \Delta t_c = \sqrt{\frac{2\rho}{c \sum_{j \in \mathcal{F}_i} V_j}}, \tag{22}$$

evaluated at the node with the largest family; see [71] for further discussion.

3 | Problem Description

Near domain boundaries and in the vicinity of internal voids or pores, the accuracy of PD models deteriorates. As schematically represented in Figure 3, material points $\mathbf{x} \in \Omega$ located within a distance δ from $\partial\Omega$ do not possess a full neighborhood: their horizon $\mathcal{H}_{\mathbf{x}}$ is truncated by the boundary. This truncation breaks the symmetry that is naturally present in the bulk, and the interior calibration of the constitutive parameters no longer holds. In BB-PD, the resulting defect manifests as a systematic *softening* (energy deficit), while in OSB-PD, the biased nonlocal dilatation introduces parity-breaking terms that can increase the modal energy relative to the corresponding full-horizon response [45].

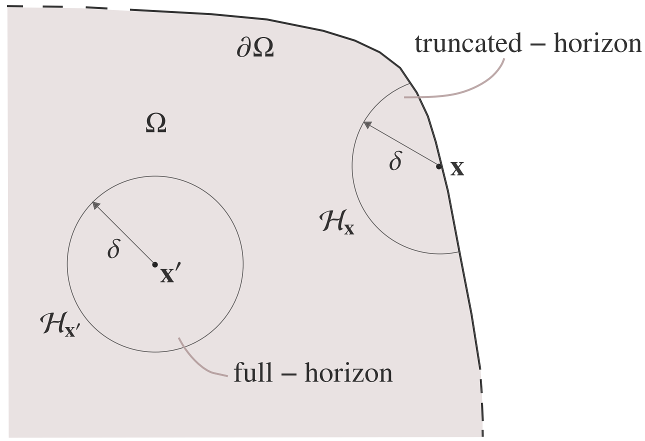

FIGURE 3 | Graphical representation of full- and truncated-horizons in a generic domain Ω described with a PD model.

To expose the algebraic root of both effects, we adopt a 1D modal analysis: a homogeneous bar with fixed horizon $\delta > 0$ is probed with harmonic test functions, and the spectral response of the BB and OSB operators is compared against the CCM reference.

For reference, the classical local operators derived from CCM are:

$$\begin{aligned} \mathcal{L}^{\mathrm{CCM}}[u](x) &:= E\,\frac{d^2u}{dx^2}, \\ \mathcal{D}^{\mathrm{CCM}}[u](x) &:= \frac{du}{dx}, \\ \mathcal{E}^{\mathrm{CCM}}[u](x) &:= \frac{1}{2}\,E\left(\frac{du}{dx}\right)^2, \end{aligned} \tag{23}$$

where $\mathcal{L}$, $\mathcal{D}$, and $\mathcal{E}$ denote the governing, derivative, and energy operators, respectively. These serve as the benchmark against which the PD operators are compared.

For the 1D BB-PD model with constant influence function ω_0 and micromodulus c, the full-horizon (subscript "FH") operators are:

$$\begin{aligned} \mathcal{L}^{\mathrm{BB}}_{\mathrm{FH}}[u](x) &:= \int_{-\delta}^{\delta} c\,\frac{u(x+\xi)-u(x)}{|\xi|}\,d\xi, \\ \mathcal{D}^{\mathrm{BB}}_{\mathrm{FH}}[u](x) &:= \int_{-\delta}^{\delta} \frac{\xi}{\delta^2}\,\frac{u(x+\xi)-u(x)}{|\xi|}\,d\xi, \\ \mathcal{E}^{\mathrm{BB}}_{\mathrm{FH}}[u](x) &:= \frac{1}{4}\int_{-\delta}^{\delta} c\,\frac{(u(x+\xi)-u(x))^2}{|\xi|}\,d\xi. \end{aligned} \tag{24}$$

For the OSB-PD model in 1D, the weighted volume and dilatation (cf. (7) and (8) with $d = 1$, $\omega = \omega_0$) are:

$$\tilde{m} := \int_{-\delta}^{\delta} \xi^2\,d\xi = \frac{2\delta^3}{3}, \qquad \overline{\theta}(x) := \frac{1}{\tilde{m}}\int_{-\delta}^{\delta} \xi\,[u(x+\xi)-u(x)]\,d\xi. \tag{25}$$

In 1D, there is no shear deformation, and the OSB energy reduces to its volumetric component $W^{\mathrm{OSB}} = a\,\overline{\theta}^2$, where a is the volumetric constitutive parameter from (10). The dilatation $\overline{\theta}$ plays the role of the strain du/dx, and the full-horizon OSB operators read:

$$\begin{aligned} \mathcal{L}^{\mathrm{OSB}}_{\mathrm{FH}}[u](x) &:= \frac{2a}{\tilde{m}}\int_{-\delta}^{\delta} \xi\,[\overline{\theta}(x)+\overline{\theta}(x+\xi)]\,d\xi, \\ \mathcal{D}^{\mathrm{OSB}}_{\mathrm{FH}}[u](x) &:= \overline{\theta}(x), \\ \mathcal{E}^{\mathrm{OSB}}_{\mathrm{FH}}[u](x) &:= a\,\overline{\theta}(x)^2. \end{aligned} \tag{26}$$

A key structural difference distinguishes the two models: in BB-PD, each bond contributes independently to the energy, whereas in OSB-PD, all bonds couple through the shared dilatation, making the energy a collective quantity.

The operators are tested with the harmonic basis function

$$\psi(x) := \exp(\mathrm{i}\alpha x), \qquad \alpha \in \mathbb{R}, \tag{27}$$

since for the linear operators $\mathcal{L}$ and $\mathcal{D}$ the response to a single plane wave fully characterizes their behavior across all wavenumbers α. The same mode is also used to compare the associated quadratic energy response. For (27) we have:

$$\psi(x+\xi) = \exp(\mathrm{i}\alpha\xi)\ \psi(x), \quad \frac{d\psi}{dx} = \mathrm{i}\alpha\ \psi, \quad \frac{d^2\psi}{dx^2} = -\ \alpha^2\psi. \tag{28}$$

The CCM modal forms are immediate:

$$\begin{aligned}
\mathcal{L}^{\mathrm{CCM}}[\psi](x) &= -\ E\alpha^2\ \exp(\mathrm{i}\alpha x),\\
\mathcal{D}^{\mathrm{CCM}}[\psi](x) &= \mathrm{i}\alpha\ \exp(\mathrm{i}\alpha x),\\
\mathcal{E}^{\mathrm{CCM}}[\psi](x) &= -\ \frac{1}{2}E\alpha^2\ \exp(2\mathrm{i}\alpha x).
\end{aligned} \tag{29}$$

The BB (full-horizon) modal forms are:

$$\begin{aligned}
\mathcal{L}^{\mathrm{BB}}_{\mathrm{FH}}[\psi](x) &= c\left(\int_{-\delta}^{\delta} \frac{\exp(\mathrm{i}\alpha\xi)-1}{|\xi|}\ d\xi\right)\exp(\mathrm{i}\alpha x),\\
\mathcal{D}^{\mathrm{BB}}_{\mathrm{FH}}[\psi](x) &= \frac{1}{\delta^2}\left(\int_{-\delta}^{\delta} \xi\ \frac{\exp(\mathrm{i}\alpha\xi)-1}{|\xi|}\ d\xi\right)\exp(\mathrm{i}\alpha x),\\
\mathcal{E}^{\mathrm{BB}}_{\mathrm{FH}}[\psi](x) &= \frac{c}{4}\left(\int_{-\delta}^{\delta} \frac{(\exp(\mathrm{i}\alpha\xi)-1)^2}{|\xi|}\ d\xi\right)\exp(2\mathrm{i}\alpha x).
\end{aligned} \tag{30}$$

For OSB-PD, substituting (27) into (25) gives $\overline{\theta}[\psi](x) = \hat{\theta}\ \psi(x)$, where

$$\hat{\theta} := \frac{1}{\tilde{m}}\int_{-\delta}^{\delta} \xi\ (\exp(\mathrm{i}\alpha\xi)-1)\ d\xi \tag{31}$$

is the spectral multiplier of the dilatation operator. On a full horizon $\int_{-\delta}^{\delta}\xi\ d\xi = 0$, so the $\overline{\theta}(x)$ term in (26) vanishes and the OSB modal forms reduce to

$$\begin{aligned}
\mathcal{L}^{\mathrm{OSB}}_{\mathrm{FH}}[\psi](x) &= 2a\ \hat{\theta}^2\ \exp(\mathrm{i}\alpha x),\\
\mathcal{D}^{\mathrm{OSB}}_{\mathrm{FH}}[\psi](x) &= \hat{\theta}\ \exp(\mathrm{i}\alpha x),\\
\mathcal{E}^{\mathrm{OSB}}_{\mathrm{FH}}[\psi](x) &= a\ \hat{\theta}^2\ \exp(2\mathrm{i}\alpha x).
\end{aligned} \tag{32}$$

For the long-wave limit ($\alpha\delta \ll 1$), we employ the symmetric horizon moments

$$\int_{-\delta}^{\delta} |\xi|^{2m-1}\ d\xi = \frac{\delta^{2m}}{m}, \qquad \int_{-\delta}^{\delta} \xi\ |\xi|^{2m-1}\ d\xi = 0, \tag{33}$$

with $m \geq 1$, which causes all odd powers of ξ to vanish. The relevant Taylor series for the BB integrands are:

$$\begin{aligned}
\frac{\exp(\mathrm{i}\alpha\xi)-1}{|\xi|} &= \mathrm{i}\alpha\ \frac{\xi}{|\xi|} - \frac{\alpha^2}{2}\ |\xi| - \frac{\mathrm{i}\alpha^3}{6}\ \xi|\xi| + \frac{\alpha^4}{24}\ |\xi|^3 + \frac{\mathrm{i}\alpha^5}{120}\ \xi|\xi|^3 - \frac{\alpha^6}{720}\ |\xi|^5 + O(|\xi|^6),\\
\xi\ \frac{\exp(\mathrm{i}\alpha\xi)-1}{|\xi|} &= \mathrm{i}\alpha\ |\xi| - \frac{\alpha^2}{2}\ \xi|\xi| - \frac{\mathrm{i}\alpha^3}{6}\ |\xi|^3 + \frac{\alpha^4}{24}\ \xi|\xi|^3 + \frac{\mathrm{i}\alpha^5}{120}\ |\xi|^5 - \frac{\alpha^6}{720}\ \xi|\xi|^5 + O(|\xi|^6),\\
\frac{(\exp(\mathrm{i}\alpha\xi)-1)^2}{|\xi|} &= -\ \alpha^2|\xi| - \mathrm{i}\alpha^3\ \xi|\xi| + \frac{7}{12}\alpha^4|\xi|^3 + \frac{\mathrm{i}\alpha^5}{4}\ \xi|\xi|^3 - \frac{31}{360}\alpha^6|\xi|^5 + O(|\xi|^6),
\end{aligned} \tag{34}$$

while for OSB-PD the integrand of $\hat{\theta}$ expands as:

$$\xi(\exp(\mathrm{i}\alpha\xi)-1)=\mathrm{i}\alpha\,\xi^2-\frac{\alpha^2}{2}\,\xi^3-\frac{\mathrm{i}\alpha^3}{6}\,\xi^4+\frac{\alpha^4}{24}\,\xi^5+\frac{\mathrm{i}\alpha^5}{120}\,\xi^6+O(\xi^7). \tag{35}$$

Inserting (34) into (30) and applying (33) yields the BB (full-horizon) modal expansions:

$$\begin{aligned}
\mathcal{L}^{\mathrm{BB}}_{\mathrm{FH}}[\psi](x)&=c\left(-\frac{\alpha^2\delta^2}{2}+\frac{\alpha^4\delta^4}{48}-\frac{\alpha^6\delta^6}{2160}+\cdots\right)\exp(\mathrm{i}\alpha x),\\
\mathcal{D}^{\mathrm{BB}}_{\mathrm{FH}}[\psi](x)&=\mathrm{i}\left(\alpha-\frac{\alpha^3\delta^2}{12}+\frac{\alpha^5\delta^4}{360}-\cdots\right)\exp(\mathrm{i}\alpha x),\\
\mathcal{E}^{\mathrm{BB}}_{\mathrm{FH}}[\psi](x)&=\frac{c}{4}\left(-\alpha^2\delta^2+\frac{7\alpha^4\delta^4}{24}-\frac{31\alpha^6\delta^6}{1080}+\cdots\right)\exp(2\mathrm{i}\alpha x).
\end{aligned} \tag{36}$$

Similarly, inserting (35) into (31) and noting that only even powers of ξ survive on the symmetric horizon (i.e., ξ^3, ξ^5, … integrate to zero), one obtains:

$$\hat{\theta}=\mathrm{i}\alpha\left(1-\frac{\alpha^2\delta^2}{10}+\frac{\alpha^4\delta^4}{280}-\cdots\right), \tag{37}$$

and the OSB (full-horizon) modal expansions:

$$\begin{aligned}
\mathcal{L}^{\mathrm{OSB}}_{\mathrm{FH}}[\psi](x)&=2a\left(-\alpha^2+\frac{\alpha^4\delta^2}{5}-\frac{3\alpha^6\delta^4}{175}+\cdots\right)\exp(\mathrm{i}\alpha x),\\
\mathcal{D}^{\mathrm{OSB}}_{\mathrm{FH}}[\psi](x)&=\mathrm{i}\left(\alpha-\frac{\alpha^3\delta^2}{10}+\frac{\alpha^5\delta^4}{280}-\cdots\right)\exp(\mathrm{i}\alpha x),\\
\mathcal{E}^{\mathrm{OSB}}_{\mathrm{FH}}[\psi](x)&=a\left(-\alpha^2+\frac{\alpha^4\delta^2}{5}-\frac{3\alpha^6\delta^4}{175}+\cdots\right)\exp(2\mathrm{i}\alpha x).
\end{aligned} \tag{38}$$

Taking the standard 1D calibrations $c=2E/\delta^2$ for BB-PD and $a=E/2$ for OSB-PD, and comparing (29) with (36) and (38), both models recover the CCM limits as $\alpha\delta\to 0$:

$$\begin{aligned}
\lim_{(\alpha\delta)\to 0}\mathcal{L}^{\mathrm{BB}}_{\mathrm{FH}}[\psi](x)&=\lim_{(\alpha\delta)\to 0}\mathcal{L}^{\mathrm{OSB}}_{\mathrm{FH}}[\psi](x)=\mathcal{L}^{\mathrm{CCM}}[\psi](x),\\
\lim_{(\alpha\delta)\to 0}\mathcal{D}^{\mathrm{BB}}_{\mathrm{FH}}[\psi](x)&=\lim_{(\alpha\delta)\to 0}\mathcal{D}^{\mathrm{OSB}}_{\mathrm{FH}}[\psi](x)=\mathcal{D}^{\mathrm{CCM}}[\psi](x),\\
\lim_{(\alpha\delta)\to 0}\mathcal{E}^{\mathrm{BB}}_{\mathrm{FH}}[\psi](x)&=\lim_{(\alpha\delta)\to 0}\mathcal{E}^{\mathrm{OSB}}_{\mathrm{FH}}[\psi](x)=\mathcal{E}^{\mathrm{CCM}}[\psi](x).
\end{aligned} \tag{39}$$

On a full horizon, both PD formulations are therefore asymptotically consistent with their CCM counterparts.

The same analysis is now carried out for a boundary node at the right end of the bar, where the PD horizon is truncated and all integrals are evaluated over $[-\delta,\ 0]$ instead of $[-\delta,\ \delta]$. The half-horizon moments are:

$$\int_{-\delta}^{0}|\xi|^{2m-1}\,d\xi=\frac{\delta^{2m}}{2m},\qquad \int_{-\delta}^{0}\xi\,|\xi|^{2m-1}\,d\xi=-\frac{\delta^{2m+1}}{2m+1}\neq 0, \tag{40}$$

with $m\geq 1$. Unlike the full-horizon case (33), the odd moments no longer vanish; consequently every power of α in the Taylor series survives upon integration, producing both real and imaginary contributions.

For BB-PD, inserting (34) into (30) with integration over $[-\delta,\ 0]$ and applying (40) gives:

$$\begin{aligned}
\mathcal{L}^{\mathrm{BB}}_{\mathrm{TH}}[\psi](x)&=c\left(-\mathrm{i}\alpha\delta-\frac{\alpha^2\delta^2}{4}+\frac{\mathrm{i}\alpha^3\delta^3}{18}+\frac{\alpha^4\delta^4}{96}-\cdots\right)\exp(\mathrm{i}\alpha x),\\
\mathcal{D}^{\mathrm{BB}}_{\mathrm{TH}}[\psi](x)&=\left(\frac{\mathrm{i}\alpha}{2}+\frac{\alpha^2\delta}{6}-\frac{\mathrm{i}\alpha^3\delta^2}{24}-\frac{\alpha^4\delta^3}{120}+\cdots\right)\exp(\mathrm{i}\alpha x),\\
\mathcal{E}^{\mathrm{BB}}_{\mathrm{TH}}[\psi](x)&=\frac{c}{4}\left(-\frac{\alpha^2\delta^2}{2}+\frac{\mathrm{i}\alpha^3\delta^3}{3}+\frac{7\alpha^4\delta^4}{48}-\cdots\right)\exp(2\mathrm{i}\alpha x).
\end{aligned} \tag{41}$$

For OSB-PD, the truncated weighted volume is $\tilde{m}_{\mathrm{TH}} = \delta^3/3$. Inserting (35) into (31) with integration limits $[-\delta,\ 0]$ yields:

$$\hat{\theta}_{\mathrm{TH}} = \mathrm{i}\alpha + \frac{3\alpha^2\delta}{8} - \frac{\mathrm{i}\alpha^3\delta^2}{10} - \frac{\alpha^4\delta^3}{48} + \frac{\mathrm{i}\alpha^5\delta^4}{280} + \cdots \tag{42}$$

Unlike the full-horizon case, where $\int_{-\delta}^{\delta} \xi\, d\xi = 0$ causes the $\overline{\theta}(x)$ term in the governing operator (26) to vanish, on the truncated-horizon $\int_{-\delta}^{0} \xi\, d\xi = -\delta^2/2 \neq 0$, producing an additional first-order contribution. The OSB truncated-horizon modal forms therefore become:

$$\begin{aligned}
\mathcal{L}_{\mathrm{TH}}^{\mathrm{OSB}}[\psi](x) &= 2a\left(\hat{\theta}_{\mathrm{TH}}^{\,2} - \frac{3}{\delta}\,\hat{\theta}_{\mathrm{TH}}\right)\exp(\mathrm{i}\alpha x),\\
\mathcal{D}_{\mathrm{TH}}^{\mathrm{OSB}}[\psi](x) &= \hat{\theta}_{\mathrm{TH}}\ \exp(\mathrm{i}\alpha x),\\
\mathcal{E}_{\mathrm{TH}}^{\mathrm{OSB}}[\psi](x) &= a\,\hat{\theta}_{\mathrm{TH}}^{\,2}\ \exp(2\mathrm{i}\alpha x).
\end{aligned} \tag{43}$$

The OSB truncated-horizon expressions (43) serve as a local diagnostic in which the same half-horizon operator is applied uniformly to isolate the algebraic effect of horizon asymmetry; in an actual boundary layer, the neighbor dilatation $\overline{\theta}(x+\xi)$ may be evaluated on a different, possibly full, horizon.

On a symmetric horizon, every full-horizon operator has a definite parity: $\mathcal{L}_{\mathrm{FH}}^{\mathrm{BB}}$ and $\mathcal{E}_{\mathrm{FH}}^{\mathrm{BB}}$ are purely real, $\mathcal{D}_{\mathrm{FH}}^{\mathrm{BB}}$ and $\hat{\theta}_{\mathrm{FH}}$ are purely imaginary. Truncation activates the odd moments in (40), injecting terms of opposite parity into every operator. The resulting errors differ qualitatively between the two models.

For BB-PD, the leading-order energy coefficient is halved: $\mathcal{E}_{\mathrm{TH}}^{\mathrm{BB}} \sim -(c/4)\,\alpha^2\delta^2/2$ compared with $-(c/4)\,\alpha^2\delta^2$ for the full-horizon. With $c = 2E/\delta^2$, this gives an energy amplitude $E\alpha^2/4$ instead of the CCM value $E\alpha^2/2$; the derivative operator is likewise halved ($\mathrm{i}\alpha/2$ vs. $\mathrm{i}\alpha$), confirming a systematic *softening*.

For OSB-PD, the imaginary (physical) part of $\hat{\theta}_{\mathrm{TH}}$ exactly equals that of $\hat{\theta}_{\mathrm{FH}}$, but truncation introduces a spurious real part. Because $|\hat{\theta}_{\mathrm{TH}}|^2 - |\hat{\theta}_{\mathrm{FH}}|^2 = 9\alpha^4\delta^2/64 + \cdots > 0$, the truncated-horizon energy exceeds the full-horizon value, producing a relative *stiffening*.

Despite their opposite signs, both defects share a common algebraic origin: the survival of odd horizon moments on the asymmetric integration domain. The same mechanism extends naturally to 2D and 3D.

In Figure 4, the foregoing analysis is quantified by plotting the norm of the energy response $\|\mathcal{E}\|$ against the nondimensional wavenumber $\alpha\delta$ for both BB and OSB models under full-horizon and truncated-horizon conditions, with $E = 1$ and $\delta = 1$. The CCM parabola $\frac{1}{2}\alpha^2$ serves as reference. As $\alpha\delta \to 0$, all energy responses vanish with order α^2; however, only the full-horizon operators recover the correct CCM coefficient, while the truncated-horizon responses retain a leading-order

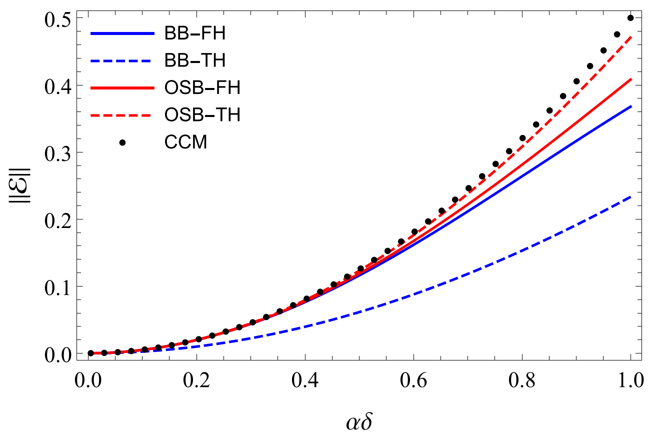

FIGURE 4 | Norm of the modal energy response $|\mathcal{E}|$ versus $\alpha\delta$ for $E = 1$, $\delta = 1$. Solid lines: full-horizon; dashed lines: truncated-horizon; circles: CCM reference. BB-PD (blue) exhibits pronounced softening upon truncation, with the truncated-horizon curve falling well below the full-horizon one. OSB-PD (red) shows the opposite trend: the truncated-horizon curve lies above the full-horizon one, indicating a relative stiffening induced by the asymmetric neighborhood. Both full-horizon models recover the CCM limit as $\alpha\delta \to 0$.

defect (cf. the discussion following (43)), confirming the local limits in (39) for the full-horizon case only. As $\alpha\delta$ increases, two contrasting behaviors emerge. In the BB formulation, the full-horizon response tracks the CCM reference over a finite spectral band, whereas the truncated-horizon response deviates immediately and remains uniformly lower, roughly halved at $\alpha\delta = 1$, reflecting the loss of half the neighborhood and the consequent energy under-counting identified in (41). In the OSB formulation, the full-horizon response nearly coincides with CCM across the full range, demonstrating the superior spectral accuracy of the SB model; however, the truncated-horizon response lies *above* the full-horizon one, exhibiting a relative stiffening caused by the surviving odd moment on the asymmetric domain, as predicted in (43). Thus, horizon truncation produces opposite spectral errors in the two formulations: BB-PD underestimates while OSB-PD overestimates the full-horizon energy. Both defects originate from the loss of symmetry of the integration domain, but manifest through different mechanisms, that is, missing bond contributions in BB-PD versus a non-vanishing first moment in OSB-PD.

4 | Solution Strategy

Recalling the discussion presented in Section 3, the PD (truncated-horizon) modal expansions in (41) and (43) reveal that the loss of horizon symmetry *activates odd horizon moments*, causing the modal forms of the governing, derivative, and energy operators ($\mathcal{L}, \mathcal{D}, \mathcal{E}$) to no longer converge to their PD (full-horizon) limits at boundary and near-boundary nodes. Hereafter, the derivation is developed in a general 3D setting; specializations to 2D and 1D are straightforward.

To restore consistency between PD (truncated-horizon) and PD (full-horizon) models, a global vector of nodal influence weights $\mathbf{w}$ is introduced, with entry w_i assigned to node $\mathbf{x}_i$. Under this framework, the BB-PD governing operator at node $\mathbf{x}_i$ is discretized as:

$$\mathbf{L}^{\mathrm{BB}}[\mathbf{u}](\mathbf{x}_i) := c \sum_{j \in \mathcal{F}_i} \left(\frac{w_j + w_i}{2} \right) \frac{\xi_j \otimes \xi_j}{\|\xi_j\|^3} (\mathbf{u}_j - \mathbf{u}_i) V_j, \tag{44}$$

where $\xi_j := \mathbf{x}_j - \mathbf{x}_i$. The corresponding discrete derivative and energy operators are then defined as follows:

$$\begin{aligned}
\mathcal{D}_x^{\mathrm{BB}}[u](\mathbf{x}_i) &:= \sum_{j \in \mathcal{F}_i} \left(\frac{w_j + w_i}{2} \right) \frac{(x_j - x_i)}{\|\xi_j\|^3} (u_j - u_i) V_j, \\
\mathcal{D}_y^{\mathrm{BB}}[u](\mathbf{x}_i) &:= \sum_{j \in \mathcal{F}_i} \left(\frac{w_j + w_i}{2} \right) \frac{(y_j - y_i)}{\|\xi_j\|^3} (u_j - u_i) V_j, \\
\mathcal{D}_z^{\mathrm{BB}}[u](\mathbf{x}_i) &:= \sum_{j \in \mathcal{F}_i} \left(\frac{w_j + w_i}{2} \right) \frac{(z_j - z_i)}{\|\xi_j\|^3} (u_j - u_i) V_j, \\
\mathcal{E}^{\mathrm{BB}}[\mathbf{u}](\mathbf{x}_i) &:= \frac{c}{4} \sum_{j \in \mathcal{F}_i} \left(\frac{w_j + w_i}{2} \right) \frac{\left((\mathbf{u}_j - \mathbf{u}_i) \cdot \xi_j\right)^2}{\|\xi_j\|^3} V_j.
\end{aligned} \tag{45}$$

For the OSB-PD formulation, the weighted discrete dilatation at node $\mathbf{x}_i$ reads:

$$\bar{\theta}_i := \frac{3}{\tilde{m}} \sum_{j \in \mathcal{F}_i} \left(\frac{w_j + w_i}{2} \right) \xi_j \cdot (\mathbf{u}_j - \mathbf{u}_i) V_j, \tag{46}$$

where $\tilde{m}$ is the analytical weighted volume of the full ball (cf. (7)) and is *not* subject to the influence weights. The discrete OSB derivative and energy operators are:

$$\begin{aligned}
\mathcal{D}_x^{\mathrm{OSB}}[u](\mathbf{x}_i) &:= \sum_{j \in \mathcal{F}_i} \left(\frac{w_j + w_i}{2} \right) \frac{(x_j - x_i)}{\|\xi_j\|^2} (u_j - u_i) V_j, \\
\mathcal{D}_y^{\mathrm{OSB}}[u](\mathbf{x}_i) &:= \sum_{j \in \mathcal{F}_i} \left(\frac{w_j + w_i}{2} \right) \frac{(y_j - y_i)}{\|\xi_j\|^2} (u_j - u_i) V_j, \\
\mathcal{D}_z^{\mathrm{OSB}}[u](\mathbf{x}_i) &:= \sum_{j \in \mathcal{F}_i} \left(\frac{w_j + w_i}{2} \right) \frac{(z_j - z_i)}{\|\xi_j\|^2} (u_j - u_i) V_j, \\
\mathcal{E}^{\mathrm{OSB}}[\mathbf{u}](\mathbf{x}_i) &:= b \sum_{j \in \mathcal{F}_i} \left(\frac{w_j + w_i}{2} \right) \frac{\left((\mathbf{u}_j - \mathbf{u}_i) \cdot \xi_j\right)^2}{\|\xi_j\|^2} V_j.
\end{aligned} \tag{47}$$

Here, b is the deviatoric constitutive parameter defined in (13); the volumetric energy contribution $a\,\overline{\theta}^2$ is implicitly accounted for through the weighted dilatation (46). The OSB governing operator follows from the weighted LPS force state (14) with $(w_j + w_i)/2$ applied to every term involving deformation differences.

In both formulations, averaging $(w_j + w_i)/2$ over each bond preserves pairwise reciprocity and yields a symmetric global stiffness matrix. The weights enter only terms that involve deformation; geometric quantities such as $\tilde{m}$ retain their analytical full-ball values and are not subject to the influence weights. The weights $\mathbf{w}$ are then determined so that, in a local test space within each neighborhood, the discrete derivative and energy operators match as closely as possible their PD (full-horizon) counterparts, thereby mitigating boundary-induced inconsistencies while retaining global symmetry.

The proposed strategy begins by *locally approximating* the nodal influence weight function $\hat{w}(\mathbf{x})$ within the neighborhood $\mathcal{H}_i$ of each node $\mathbf{x}_i$ using the following polynomial basis expansion:

$$\hat{w}(\mathbf{x}) = \sum_{k=1}^{n_p} a_k\; p_k(\mathbf{x}) = \mathbf{p}^\top(\mathbf{x})\;\mathbf{a}, \quad \mathbf{x} \in \mathcal{H}_i, \tag{48}$$

where $n_p := |\mathbf{p}|$ denotes the number of polynomial basis functions. The basis and coefficient vectors are given, respectively, by:

$$\mathbf{p}(\mathbf{x}) = \left[\, 1,\ \frac{x}{\delta},\ \frac{y}{\delta},\ \frac{z}{\delta},\ \frac{x^2}{\delta^2},\ \frac{xy}{\delta^2},\ \frac{xz}{\delta^2},\ \frac{y^2}{\delta^2},\ \frac{yz}{\delta^2},\ \frac{z^2}{\delta^2},\ \dots \,\right]^\top, \qquad \mathbf{a} = [\ a_1,\ a_2,\ \dots,\ a_{n_p}\ ]^\top. \tag{49}$$

Here, the vector $\mathbf{a}$ collects the unknown expansion coefficients, which are to be determined such that the local approximation reproduces the desired values of the weight function at the nodal locations. To determine the coefficient vector $\mathbf{a}$, a local fitting problem is formulated to enforce the consistency of the reconstructed influence function with the nodal weights, as well as with the target derivative and energy operators. This leads to the following least-squares minimization:

$$\min_{\mathbf{a}} \|\mathbf{M}_{\mathrm{c}}\mathbf{a} - \mathbf{w}_{\mathcal{F}}\|_2^2 + \left\|\mathbf{M}_{\mathcal{D}_x}\mathbf{a} - \mathbf{d}_x^\star\right\|_2^2 + \left\|\mathbf{M}_{\mathcal{D}_y}\mathbf{a} - \mathbf{d}_y^\star\right\|_2^2 + \left\|\mathbf{M}_{\mathcal{D}_z}\mathbf{a} - \mathbf{d}_z^\star\right\|_2^2 + \|\mathbf{M}_{\mathcal{E}}\mathbf{a} - \mathbf{e}^\star\|_2^2. \tag{50}$$

Here, each $\mathbf{M}$ denotes a moment matrix associated with a specific matching condition, whose explicit form will be introduced below. Specifically, $\mathbf{M}_{\mathrm{c}}$ enforces the collocation of the polynomial expansion at the neighboring nodes in $\mathcal{F}_i$, with the vector $\mathbf{w}_{\mathcal{F}}$ collecting the weight values w_j of the family nodes. In addition, $\mathbf{M}_{\mathcal{D}_x}$, $\mathbf{M}_{\mathcal{D}_y}$, $\mathbf{M}_{\mathcal{D}_z}$, and $\mathbf{M}_{\mathcal{E}}$ encode the consistency requirements for the x-, y-, z-derivative and energy operators, respectively, with the corresponding right-hand side vectors $\mathbf{d}_x^\star$, $\mathbf{d}_y^\star$, $\mathbf{d}_z^\star$, and $\mathbf{e}^\star$ containing the target values prescribed by the PD (full-horizon) operators on a chosen test space.

For each node $\mathbf{x}_i$, the collocation matrix $\mathbf{M}_{\mathrm{c}}$ and the associated data vector $\mathbf{w}_{\mathcal{F}}$ are given, respectively, by:

$$\mathbf{M}_{\mathrm{c}} = \left[\mathbf{p}^\top(\xi_j)\right]_{j\in\mathcal{F}_i} \equiv \begin{bmatrix} \mathbf{p}^\top(\xi_{j_1}) \\ \mathbf{p}^\top(\xi_{j_2}) \\ \vdots \\ \mathbf{p}^\top(\xi_{j_{n_{\mathcal{F}_i}}}) \end{bmatrix} \in \mathbb{R}^{\,n_{\mathcal{F}_i}\times n_p}, \qquad \mathbf{w}_{\mathcal{F}} = \begin{bmatrix} w_{j_1} \\ w_{j_2} \\ \vdots \\ w_{j_{n_{\mathcal{F}_i}}} \end{bmatrix} \in \mathbb{R}^{\,n_{\mathcal{F}_i}}, \tag{51}$$

where $\{j_1, j_2, \dots, j_{n_{\mathcal{F}_i}}\}$ denotes an enumeration of the family $\mathcal{F}_i$ and $n_{\mathcal{F}_i} := |\mathcal{F}_i|$ is the number of family nodes of $\mathbf{x}_i$.

To enforce the matching conditions for the derivative and energy operators, two test sets are introduced: (i) a horizon-scaled *scalar* polynomial basis for the derivative operators, and (ii) its *vector* lift (via Cartesian unit vectors) for the energy operator. For the derivative operators, the scalar test basis is:

$$\mathcal{T}(\mathbf{x}) = \left\{\phi_m(\mathbf{x})\right\}_{m=1}^{n_T} = \left\{\ 1, \frac{x}{\delta}, \frac{y}{\delta}, \frac{z}{\delta}, \frac{x^2}{\delta^2}, \frac{xy}{\delta^2}, \frac{xz}{\delta^2}, \frac{y^2}{\delta^2}, \frac{yz}{\delta^2}, \frac{z^2}{\delta^2}, \dots \right\}, \tag{52}$$

where $n_T := |\mathcal{T}|$ denotes the number of scalar tests. For the energy operator, the same scalars are lifted to vector fields through multiplication by the Cartesian unit vectors $\mathbf{e}_l$:

$$\mathcal{T}_E(\mathbf{x}) = \left\{\ \phi_m(\mathbf{x})\ \mathbf{e}_l \,|\, \phi_m \in \mathcal{T},\ l \in \{x, y, z\}\right\}. \tag{53}$$

Equivalently, the first few elements read:

$$\left\{\begin{bmatrix}1\\0\\0\end{bmatrix},\begin{bmatrix}0\\1\\0\end{bmatrix},\begin{bmatrix}0\\0\\1\end{bmatrix},\frac{x}{\delta}\begin{bmatrix}1\\0\\0\end{bmatrix},\frac{x}{\delta}\begin{bmatrix}0\\1\\0\end{bmatrix},\frac{x}{\delta}\begin{bmatrix}0\\0\\1\end{bmatrix},\dots\right\}.$$

By construction, $|\mathcal{T}_E| = 3\, n_T$. Given that, in principle, n_T can be chosen up to any polynomial order, it is here set to $n_T = n_p$ to match the polynomial basis used in the weight approximation (48).

To assemble the operator blocks in (50), we introduce the kernel exponent

$$q := \begin{cases} 3 & \text{BB-PD,} \\ 2 & \text{OSB-PD,} \end{cases} \tag{54}$$

which encodes the only structural difference between the two formulations in the moment matrices that follow.

For the x-derivative operator block, we employ the scalar-valued tests $\mathcal{T} = \{\phi_k\}_{k=1}^{n_T}$. The corresponding consistency vector entering (50) is:

$$\mathbf{M}_{\mathcal{D}_x}\mathbf{a} = \left[\ \mathcal{D}_x^{\mathrm{BB/OSB}}[\phi_k](\mathbf{0})\ \right]_{k=1}^{n_T} \equiv \begin{bmatrix} \mathcal{D}_x^{\mathrm{BB/OSB}}[\phi_1](\mathbf{0}) \\ \mathcal{D}_x^{\mathrm{BB/OSB}}[\phi_2](\mathbf{0}) \\ \vdots \\ \mathcal{D}_x^{\mathrm{BB/OSB}}[\phi_{n_T}](\mathbf{0}) \end{bmatrix}, \tag{55}$$

where the superscript BB/OSB indicates that either the BB operator (45) or the OSB operator (47) is employed. Substituting the local weight approximation (48) into the discrete derivative operator, the moment matrix $\mathbf{M}_{\mathcal{D}_x} \in \mathbb{R}^{\,n_T \times n_p}$ is defined row-wise by:

$$\mathbf{M}_{\mathcal{D}_x} := \left[\ \sum_{j\in\mathcal{F}_i} \frac{\mathbf{p}^\top(\xi_j)+\mathbf{p}^\top(\mathbf{0})}{2}\ \frac{(x_j - x_i)}{\|\xi_j\|^q}\ \left(\phi_k(\xi_j)-\phi_k(\mathbf{0})\right)\ V_j\ \right]_{k=1}^{n_T}. \tag{56}$$

In complete analogy, the y- and z-derivative moment matrices $\mathbf{M}_{\mathcal{D}_y}$, $\mathbf{M}_{\mathcal{D}_z} \in \mathbb{R}^{\,n_T \times n_p}$ are defined row-wise by:

$$\begin{aligned} \mathbf{M}_{\mathcal{D}_y} &:= \left[\ \sum_{j\in\mathcal{F}_i} \frac{\mathbf{p}^\top(\xi_j)+\mathbf{p}^\top(\mathbf{0})}{2}\ \frac{(y_j - y_i)}{\|\xi_j\|^q}\ \left(\phi_k(\xi_j)-\phi_k(\mathbf{0})\right)\ V_j\ \right]_{k=1}^{n_T}, \\ \mathbf{M}_{\mathcal{D}_z} &:= \left[\ \sum_{j\in\mathcal{F}_i} \frac{\mathbf{p}^\top(\xi_j)+\mathbf{p}^\top(\mathbf{0})}{2}\ \frac{(z_j - z_i)}{\|\xi_j\|^q}\ \left(\phi_k(\xi_j)-\phi_k(\mathbf{0})\right)\ V_j\ \right]_{k=1}^{n_T}. \end{aligned} \tag{57}$$

For the energy operator, we employ the vector-valued tests $\mathcal{T}_E = \{\mathbf{\Phi}_k\}_{k=1}^{3n_T} = \{\phi_m\,\mathbf{e}_l\ :\ \phi_m \in \mathcal{T},\ l \in \{x,y,z\}\}$. The corresponding consistency vector in (50) reads:

$$\mathbf{M}_{\mathcal{E}}\mathbf{a} = \left[\ \mathcal{E}^{\mathrm{BB/OSB}}[\mathbf{\Phi}_k](\mathbf{0})\ \right]_{k=1}^{3n_T} \equiv \begin{bmatrix} \mathcal{E}^{\mathrm{BB/OSB}}[\mathbf{\Phi}_1](\mathbf{0}) \\ \mathcal{E}^{\mathrm{BB/OSB}}[\mathbf{\Phi}_2](\mathbf{0}) \\ \vdots \\ \mathcal{E}^{\mathrm{BB/OSB}}[\mathbf{\Phi}_{3n_T}](\mathbf{0}) \end{bmatrix}, \tag{58}$$

and the associated moment matrix $\mathbf{M}_{\mathcal{E}} \in \mathbb{R}^{\,3n_T \times n_p}$ is defined row-wise as:

$$\mathbf{M}_{\mathcal{E}} := \left[\ \sum_{j\in\mathcal{F}_i} \frac{\mathbf{p}^\top(\xi_j)+\mathbf{p}^\top(\mathbf{0})}{2}\ \frac{\left((\mathbf{\Phi}_k(\xi_j)-\mathbf{\Phi}_k(\mathbf{0}))\cdot\xi_j\right)^2}{\|\xi_j\|^q}\ V_j\ \right]_{k=1}^{3n_T}. \tag{59}$$

In both blocks, the factor $(\mathbf{p}^\top(\xi_j)+\mathbf{p}^\top(\mathbf{0}))/2$ encodes the bond-averaged weight $(w_j + w_i)/2$ through the polynomial approximation (48).

Remark 1. For the OSB-PD formulation, no separate dilatation constraint appears in the least-squares problem (50). However, the computed weights are applied to the discrete dilatation (46) during the solution procedure. Replacing $\tilde{m}$ by its analytical full-ball value removes the leading source of volumetric inconsistency, and the derivative and energy blocks, which target the deviatoric kernel $\|\xi\|^{-2}$, provide sufficient correction for the deviatoric force state; the dilatation then benefits from the improved weights without requiring an explicit fitting constraint.

In order to construct the target vectors, continuous operators defined by integration over the full ball B_δ of radius δ are introduced. Given that the considered test functions are polynomials, these integrals can be evaluated analytically.

For BB-PD, the continuous full-ball derivative and energy operators read:

$$\begin{aligned}
\mathcal{D}_x^{\mathrm{BB,Ball}}[u](\mathbf{x}) &:= \int_{B_\delta} \frac{\xi_x}{\|\xi\|^3}(u(\mathbf{x}+\xi)-u(\mathbf{x}))\, dV_\xi,\\
\mathcal{D}_y^{\mathrm{BB,Ball}}[u](\mathbf{x}) &:= \int_{B_\delta} \frac{\xi_y}{\|\xi\|^3}(u(\mathbf{x}+\xi)-u(\mathbf{x}))\, dV_\xi,\\
\mathcal{D}_z^{\mathrm{BB,Ball}}[u](\mathbf{x}) &:= \int_{B_\delta} \frac{\xi_z}{\|\xi\|^3}(u(\mathbf{x}+\xi)-u(\mathbf{x}))\, dV_\xi,\\
\mathcal{E}^{\mathrm{BB,Ball}}[\mathbf{u}](\mathbf{x}) &:= \frac{c}{4}\int_{B_\delta} \frac{((\mathbf{u}(\mathbf{x}+\xi)-\mathbf{u}(\mathbf{x}))\cdot\xi)^2}{\|\xi\|^3}\, dV_\xi.
\end{aligned} \tag{60}$$

For OSB-PD, the corresponding operators are:

$$\begin{aligned}
\mathcal{D}_x^{\mathrm{OSB,Ball}}[u](\mathbf{x}) &:= \int_{B_\delta} \frac{\xi_x}{\|\xi\|^2}(u(\mathbf{x}+\xi)-u(\mathbf{x}))\, dV_\xi,\\
\mathcal{D}_y^{\mathrm{OSB,Ball}}[u](\mathbf{x}) &:= \int_{B_\delta} \frac{\xi_y}{\|\xi\|^2}(u(\mathbf{x}+\xi)-u(\mathbf{x}))\, dV_\xi,\\
\mathcal{D}_z^{\mathrm{OSB,Ball}}[u](\mathbf{x}) &:= \int_{B_\delta} \frac{\xi_z}{\|\xi\|^2}(u(\mathbf{x}+\xi)-u(\mathbf{x}))\, dV_\xi,\\
\mathcal{E}^{\mathrm{OSB,Ball}}[\mathbf{u}](\mathbf{x}) &:= b\int_{B_\delta} \frac{((\mathbf{u}(\mathbf{x}+\xi)-\mathbf{u}(\mathbf{x}))\cdot\xi)^2}{\|\xi\|^2}\, dV_\xi.
\end{aligned} \tag{61}$$

Based on the previously introduced operators and on the test functions defined in (52) and (53), the target vectors prescribed by the PD (full-horizon) formulation are:

$$\begin{aligned}
\mathbf{d}_x^\star &= \left[\mathcal{D}_x^{\mathrm{Ball}}[\phi_k](\mathbf{0})\right]_{k=1}^{n_T},\\
\mathbf{d}_y^\star &= \left[\mathcal{D}_y^{\mathrm{Ball}}[\phi_k](\mathbf{0})\right]_{k=1}^{n_T},\\
\mathbf{d}_z^\star &= \left[\mathcal{D}_z^{\mathrm{Ball}}[\phi_k](\mathbf{0})\right]_{k=1}^{n_T},\\
\mathbf{e}^\star &= \left[\mathcal{E}^{\mathrm{Ball}}[\boldsymbol{\Phi}_k](\mathbf{0})\right]_{k=1}^{3n_T}.
\end{aligned} \tag{62}$$

Remark 2. The material parameters (e.g., the micromodulus c for the BB model, or a and b for the OSB model) enter both the moment matrices and the target vectors as common multiplicative factors; they therefore cancel after per-row normalization and do not affect the resulting weights. Consequently, the targets $\mathbf{d}_x^\star$, $\mathbf{d}_y^\star$, $\mathbf{d}_z^\star$, and $\mathbf{e}^\star$ are purely geometric quantities, each expressible in closed form through the d-dimensional ball moment

$$\mathcal{I}_q(\mathbf{r}) = \int_{\|\xi\|\le\delta} \frac{\xi_1^{r_1}\cdots\xi_d^{r_d}}{\|\xi\|^q}\, \mathrm{d}V, \tag{63}$$

which evaluates to a product of Gamma functions whenever all exponents r_i are even, and vanishes otherwise. The complete set of 3D target vectors for the BB and OSB models is implemented in the open-source package `perifit` [63].

Collecting all constraints, the local fitting problem at node $\mathbf{x}_i$ takes the compact form

$$\min_{\mathbf{a}} \|\mathbf{M}\,\mathbf{a}-\mathbf{b}^\star\|_2^2 + \lambda\,\|\mathbf{a}\|_2^2, \tag{64}$$

where

$$\mathbf{M} = \begin{bmatrix} \mathbf{M}_c \\ \mathbf{M}_{\mathcal{D}_x} \\ \mathbf{M}_{\mathcal{D}_y} \\ \mathbf{M}_{\mathcal{D}_z} \\ \mathbf{M}_{\mathcal{E}} \end{bmatrix}, \qquad \mathbf{b}^\star = \begin{bmatrix} \mathbf{w}_{\mathcal{F}} \\ \mathbf{d}_x^\star \\ \mathbf{d}_y^\star \\ \mathbf{d}_z^\star \\ \mathbf{e}^\star \end{bmatrix}, \tag{65}$$

and $\lambda \geq 0$ is a small Tikhonov regularization parameter that prevents ill-conditioning when the local moment matrix is nearly rank-deficient (e.g., near boundaries or irregular point distributions). In practice, λ is chosen adaptively as a small fraction of the largest diagonal entry of $\mathbf{M}^\top \mathbf{M}$.

Since the system is generally overdetermined, the regularized minimizer is:

$$\mathbf{a} = \left(\mathbf{M}^\top \mathbf{M} + \lambda\, \mathbf{I}\right)^{-1} \mathbf{M}^\top\, \mathbf{b}^\star, \tag{66}$$

which reduces to the Moore–Penrose pseudoinverse $\mathbf{M}^{+}\mathbf{b}^\star$ when $\lambda = 0$, consistent with established meshfree formulations [72–76]. Partitioning the resulting generalized inverse into blocks corresponding to each constraint group,

$$\left(\mathbf{M}^\top \mathbf{M} + \lambda\, \mathbf{I}\right)^{-1} \mathbf{M}^\top = \left[\mathbf{N}_c\ \ \mathbf{N}_{\mathcal{D}_x}\ \ \mathbf{N}_{\mathcal{D}_y}\ \ \mathbf{N}_{\mathcal{D}_z}\ \ \mathbf{N}_{\mathcal{E}}\right], \tag{67}$$

the reconstructed influence weight function $\hat{w}(\mathbf{x})$ within the horizon $\mathcal{H}_i$ reads:

$$\hat{w}_i(\xi) = \mathbf{p}(\xi)^\top \left(\mathbf{N}_c\ \mathbf{w}_{\mathcal{F}} + \mathbf{N}_{\mathcal{D}_x}\ \mathbf{d}_x^\star + \mathbf{N}_{\mathcal{D}_y}\ \mathbf{d}_y^\star + \mathbf{N}_{\mathcal{D}_z}\ \mathbf{d}_z^\star + \mathbf{N}_{\mathcal{E}}\ \mathbf{e}^\star\right). \tag{68}$$

For each node $\mathbf{x}_i$, this local procedure relates the unknown nodal weights of the family $\mathcal{F}_i$ to the target conditions. Assembling over all nodes $i = 1, \ldots, N$ yields the global sparse linear system

$$\mathbf{K}_w\ \mathbf{w} = \mathbf{F}_w, \tag{69}$$

where $\mathbf{K}_w$ is the global influence matrix assembled from the local collocation matrices, and $\mathbf{F}_w$ collects the contributions of the target vectors $\mathbf{d}_x^\star$, $\mathbf{d}_y^\star$, $\mathbf{d}_z^\star$, $\mathbf{e}^\star$ across all neighborhoods. The system is sparse by construction, as each row involves only the weights of the local family $\mathcal{F}_i$, and is solved using a standard sparse solver. The resulting weight vector $\mathbf{w}$ is then employed in the discrete PD operators (45) and (47).

Remark 3. Because the target vectors $\mathbf{d}_x^\star$, $\mathbf{d}_y^\star$, $\mathbf{d}_z^\star$, and $\mathbf{e}^\star$ are evaluated analytically over full balls, the calibration naturally corrects the effective volume integration at *all* nodes, that is, not only those near boundaries. Interior nodes with full neighborhoods also benefit, since the discrete quadrature is matched against exact full-horizon values. The method thus provides a consistent integration refinement throughout the entire domain.

Remark 4. The operator matching is formulated on the linearized PD kernels (cf. (45–47)), but the resulting weights correct the geometric structure of the discrete integration, specifically the bond-averaged volume contributions, rather than the constitutive response. Consequently, the same nodal weights w_i remain valid when the full nonlinear force law (e.g., the PMB model (16)) is employed: the weights compensate for the missing or imbalanced bond contributions regardless of the strain level or constitutive nonlinearity.

Remark 5. Energetically consistent surface-correction methods assign direction-dependent amplification factors to individual bonds so that the PD strain energy matches a local (affine) reference deformation, even under truncated neighborhoods [50]. The present approach differs in three respects: (i) it calibrates PD operators against their own full-horizon counterparts rather than against a CCM reference solution; (ii) it introduces per-node *scalar* weights entering each bond symmetrically as $(w_j + w_i)/2$, preserving the symmetry of the global stiffness matrix by construction; and (iii) it does not require boundary tractions, ray–surface distance calculations, or fictitious/ghost layers.

Remark 6. The global system (69) is sparse by construction: each row involves only the local family $\mathcal{F}_i$. Assembly is performed in parallel over nodes with cost proportional to the total number of bonds. Standard iterative solvers (e.g., conjugate gradients or GMRES with diagonal or incomplete Cholesky preconditioning) converge rapidly. When memory is constrained, a matrix-free implementation applies the operator on the fly from the stored neighborhoods, avoiding explicit matrix assembly while producing the same solution.

Remark 7. In the crack propagation test presented in Section 5.4, the PMB critical stretch s_0 from (18) is used without modification. Since the target vectors are evaluated for a full, symmetric horizon with $\omega = \omega_0$, the weighted operators are constructed to reproduce the same full-horizon energetics. Re-estimating s_0 for a truncated-horizon would therefore double-count the surface correction.

Remark 8. Influence-weight optimization shares conceptual links with accuracy-enhancement techniques for nonlocal discretizations, such as reproducing-kernel PD (RK-PD) and asymptotically compatible meshfree quadrature [77, 78]. The present method, however, leaves the PD kinematics and operators unchanged and compensates horizon truncation solely through symmetric node-wise scalar weights, enforcing pairwise reciprocity by construction. Moreover, the weights are determined by PD-to-PD operator matching against analytic full-horizon values, rather than by local CCM-limit reproduction requirements.

The proposed strategy integrates seamlessly with existing PD codes: nodal influence weights $\mathbf{w}$ are computed once in a load-independent preprocessing step and then applied as symmetric bond scalings. A ready-to-use implementation is provided in the open-source Python package `perifit` [63], which takes as input the nodal coordinates, the horizon δ, and the family lists $\{\mathcal{F}_i\}$, and returns the weight vector $\mathbf{w}$ along with the coupling coefficients needed for the global system (69). Internally, the package evaluates full-horizon targets via closed-form ball moments (63), assembles per-node moment matrices with Tikhonov regularization, and performs per-row normalization so that material parameters need not be specified. The procedure is summarized below.

1. *Families*: For each node $\mathbf{x}_i$, build $\mathcal{F}_i = \{\ j\ :\ 0 < \|\boldsymbol{\xi}_j\| \leq \delta\ \}$ with $\boldsymbol{\xi}_j := \mathbf{x}_j - \mathbf{x}_i$.
2. *Basis, tests, and targets*: Adopt the polynomial basis $\mathbf{p}(\boldsymbol{\xi})$ (49), the scalar test set $\mathcal{T}$ (52), and the vector tests $\mathcal{T}_E$ (53). Evaluate the full-horizon target vectors $\mathbf{d}_x^\star$, $\mathbf{d}_y^\star$, $\mathbf{d}_z^\star$, and $\mathbf{e}^\star$ analytically via ball moments (63) as defined in (62).
3. *Local moment matrices*: At each node $\mathbf{x}_i$, assemble $\mathbf{M}_c$ (51), $\mathbf{M}_{\mathcal{D}_x}$ (56), $\mathbf{M}_{\mathcal{D}_y}$, $\mathbf{M}_{\mathcal{D}_z}$ (57), and $\mathbf{M}_{\mathcal{E}}$ (59); stack into $\mathbf{M}$ (65) and compute the regularized inverse (66).
4. *Row extraction*: Partition the inverse as in (67) and evaluate the reconstruction (68) at $\boldsymbol{\xi} = \mathbf{0}$ to obtain the coupling coefficients $\overline{\boldsymbol{\gamma}}_i^{\top} := \mathbf{p}(\mathbf{0})^{\top}\mathbf{N}_c$ and the right-hand side contribution $\overline{f}_i := \mathbf{p}(\mathbf{0})^{\top}\left(\mathbf{N}_{\mathcal{D}_x}\mathbf{d}_x^\star + \mathbf{N}_{\mathcal{D}_y}\mathbf{d}_y^\star + \mathbf{N}_{\mathcal{D}_z}\mathbf{d}_z^\star + \mathbf{N}_{\mathcal{E}}\mathbf{e}^\star\right)$.
5. *Assembly*: Insert the row relation $w_i - \sum_{\ell \in \mathcal{F}_i} \overline{\gamma}_{i\ell}\ w_\ell = \overline{f}_i$ into the sparse global system $\mathbf{K}_w\ \mathbf{w} = \mathbf{F}_w$ (69).
6. *Solve*: Solve (69) for $\mathbf{w}$; the result is load-independent.
7. *Bond scaling*: For each bond (i, j), replace the constitutive prefactor by its weighted counterpart, for example, $\overline{c}_{ij} = c\ (w_j + w_i)/2$ for BB-PD (44) and (45) or the analogous scaling for OSB-PD (46) and (47), and proceed with the time integration or static solve.

5 | Numerical Examples

The proposed approach, hereinafter referred to as *modified-PD*, is evaluated on six numerical examples; the standard PD formulation without any surface correction is referred to as simply as *PD*. Examples 1–4 employ the BB-PD formulation exclusively, while Examples 5 and 6 include both BB-PD and OSB-PD. All examples except Example 4 are formulated in a dimensionless setting; Example 4 employs physical material parameters and includes failure analysis.

Examples 1–3, and 5 are static problems with exact CCM solutions against which a δ-convergence study is performed. Example 4 is a dynamic fracture problem; the modified-PD solution is compared with a high-resolution standard PD reference on a fine grid. Examples 5 and 6 additionally assess the computational cost of the weight calibration and verify that the system (69) remains well-conditioned under mesh refinement.

The weight calibration uses the open-source Python package `perifit` [63] (Python 3.10) with BiCGSTAB solver (tolerance 10^{-10}). Reference PD simulations employ C++ solvers. The wall time in Examples 5 and 6 measures assembly and iterative solution of $\mathbf{K}_w\,\mathbf{w} = \mathbf{F}_w$, averaged over three runs. All computations use a single core of an Intel Core i7-8700 at 3.20 GHz with 16 GB RAM.

In all examples, both the interpolation bases and the test function sets employ horizon-scaled monomials up to the second order. The relative L^2 displacement error is defined as:

$$e_u := \left(\frac{\sum_i \left\| \mathbf{u}_i - \mathbf{u}_i^{\text{ref}} \right\|^2}{\sum_i \left\| \mathbf{u}_i^{\text{ref}} \right\|^2} \right)^{1/2}, \tag{70}$$

where the summation runs over all nodes in the domain and $\|\cdot\|$ denotes the Euclidean norm of the displacement vector.

5.1 | Example 1: 1D Bar Under Uniaxial Tension

A unit-length bar ($L = 1$) with Young's modulus $E = 1$ and exact reference displacement $u^{\text{ref}}(x) = x$ (no body force) is considered. The left end ($x = 0$) is constrained, and a concentrated traction $P = 1$ is applied at the right end ($x = 1$); both conditions are imposed at a single node to isolate boundary effects (see Figure 5).

A δ-convergence study [66, 69] is performed for $m_{\text{ratio}} = \delta/\Delta x \in \{4,\ 8,\ 16\}$. The results, reported in Figure 6, show that the modified-PD model exhibits strictly monotonic error decay and consistently lower errors than PD across all values of m_{ratio}. In contrast, PD does not decrease monotonically for $m_{\text{ratio}} = 4$ and 8, which is attributed to the combined effect of unmodified midpoint quadrature [52, 69, 79] and boundary-induced softening. The modified-PD approach regularizes this convergence behavior by calibrating the nodal influence weights to satisfy the operator-matching constraints, thereby suppressing the discretization artifacts that cause the irregular error decay in PD.

For the representative case $\Delta x = 0.005$ and $m_{\text{ratio}} = 4$, Figure 7 (top) shows that the modified-PD displacement follows the exact solution more closely and enforces the boundary conditions at the bar ends better than PD. Figure 7 (bottom) reports the nodal influence weights w for $m_{\text{ratio}} \in \{4,\ 8,\ 16\}$. In all cases, the weights form a boundary layer: they are amplified near the bar ends, where horizons are truncated, and slightly reduced just inside the domain. As m_{ratio} increases, the boundary layer narrows and the interior weights approach unity, because a larger horizon encompasses more neighbors and the relative loss due to truncation diminishes. This behavior stems from the least-squares fit of the derivative and energy matching constraints: At truncated-horizons the system compensates for missing neighbors by increasing local weights, while the finite-dimensional fit distributes the residual smoothly. The resulting pattern counteracts boundary-induced softening and improves boundary-condition enforcement.

5.2 | Example 2: Cantilever Beam With End Shear

A 2D cantilever beam of length $L = 1$, height $H = 1$, unit thickness, Young's modulus $E = 1$, and Poisson's ratio $\nu = 1/3$ (plane stress) is considered (see Figure 8). The top and bottom edges are traction-free; the left edge ($x = 0$) is supported at three discrete points (upper, middle, lower), and the right edge ($x = L$) carries a parabolic end shear:

$$t_x(L, y) = 0, \qquad t_y(L, y) = \frac{6P}{H^3}\, y\,(H - y), \tag{71}$$

with resultant $P = 1$. The exact CCM reference solution is:

$$u_x^{\text{ref}}(x, y) = \frac{P}{6EI_b}\left(y - \frac{H}{2}\right)\left[\left(6Lx - 3x^2\right) + (2 + \nu)\left(y^2 - Hy\right)\right], \tag{72}$$

$$u_y^{\text{ref}}(x, y) = -\frac{P}{6EI_b}\left[\left(3Lx^2 - x^3\right) + 3\nu(L - x)\left(y - \frac{H}{2}\right)^2 + \frac{(4 + 5\nu)H^2}{4}\,x\right], \tag{73}$$

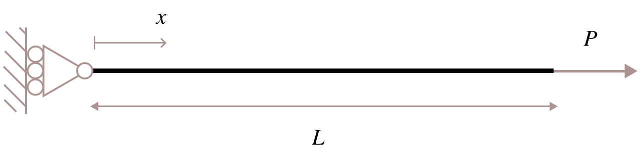

FIGURE 5 | Schematic representation of the problem domain and boundary conditions in Example 1.

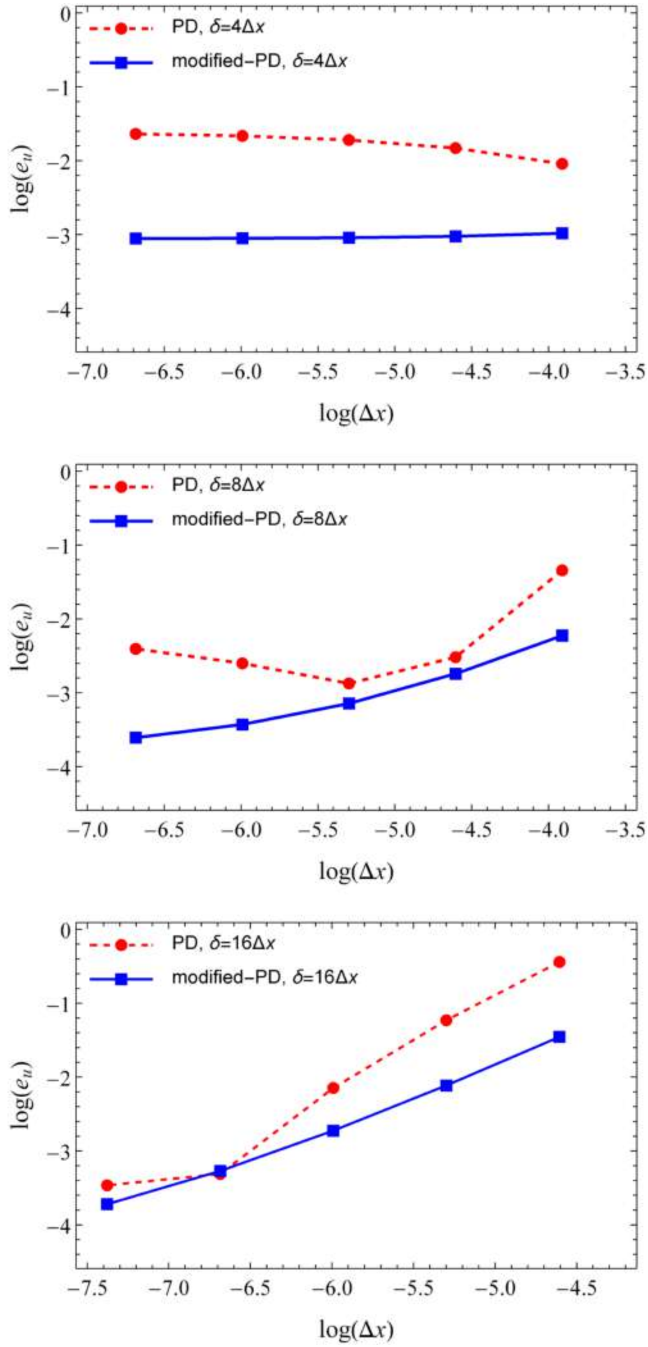

FIGURE 6 | δ-convergence study for Example 1: $\log(e_u)$ versus $\log(\Delta x)$ for PD (red, dashed) and modified-PD (blue, solid) with $m_{\text{ratio}} \in \{4,\ 8,\ 16\}$.

where $I_b = H^3/12$.

A δ-convergence study is performed at fixed $m_{\text{ratio}} = 4$ for $\Delta x \in \{0.04,\ 0.02,\ 0.01,\ 0.005\}$. Figure 9 (top) shows that modified-PD attains substantially lower errors and a steeper decay rate than PD. Figure 9 (bottom) reports the vertical displacement u_y along the midline $y = H/2$ for the representative case $\Delta x = 0.01$: modified-PD closely follows the exact solution, whereas PD exhibits a larger deviation.

Figure 10 displays the nodal influence weights $w(x, y)$ for $\Delta x = 0.01$ and $m_{\text{ratio}} = 4$. The weights are amplified near the boundaries, compensating for horizon truncation, and slightly reduced in the interior, where the correction primarily improves volume integration accuracy.

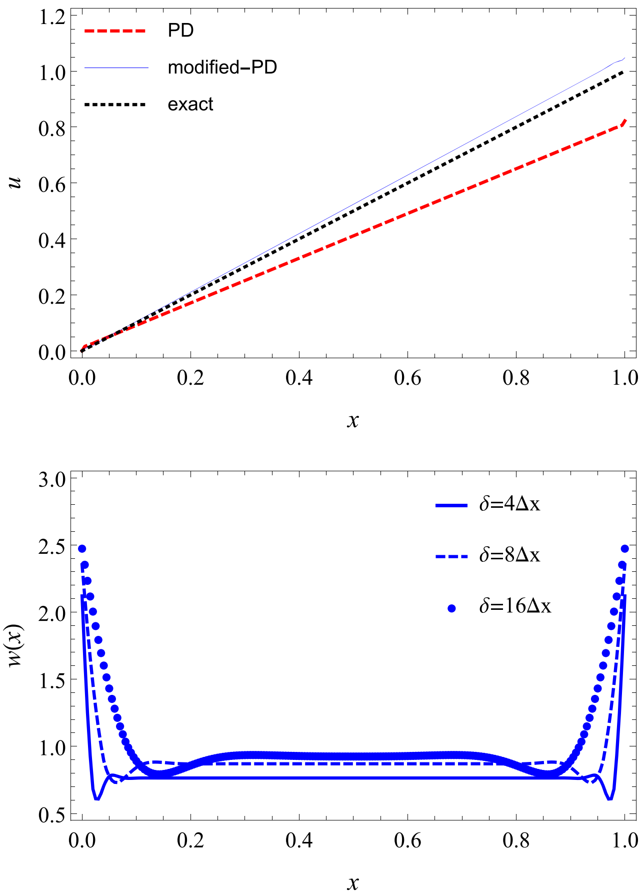

FIGURE 7 | Top: displacement $u(x)$ for PD (red, dashed), modified-PD (blue, solid), and the exact solution $u^{\mathrm{ref}}(x) = x$ (black, dashed). Bottom: nodal influence weights w for $m_{\mathrm{ratio}} \in \{4,\ 8,\ 16\}$ ($\Delta x = 0.005$). As m_{ratio} increases, the boundary layer narrows and interior weights tend toward unity.

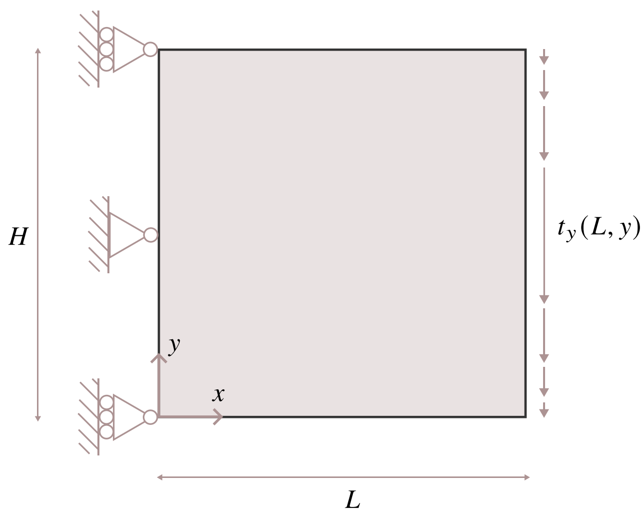

FIGURE 8 | Schematic representation of the problem domain and boundary conditions in Example 2.

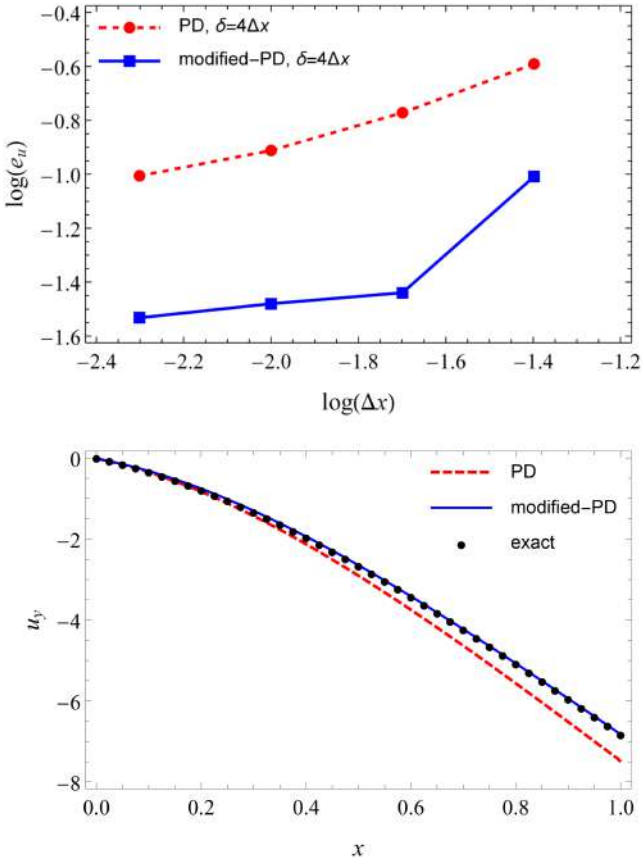

FIGURE 9 | Top: δ-convergence at fixed $m_{\text{ratio}} = 4$: $\log(e_u)$ vs. $\log(\Delta x)$ for PD (red, dashed) and modified-PD (blue, solid). Bottom: u_y along the midline $y = H/2$ for PD (red, dashed), modified-PD (blue, solid), and the exact solution (73) (black circles) with $\Delta x = 0.01$.

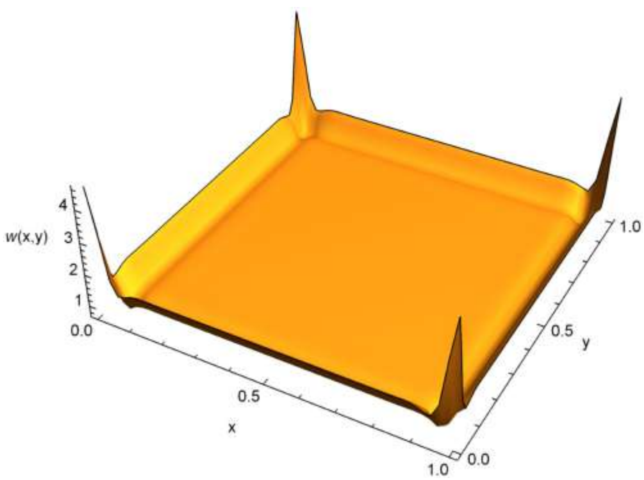

FIGURE 10 | Nodal influence weights $w(x, y)$ for Example 2 with $\Delta x = 0.01$ and $m_{\text{ratio}} = 4$.

To verify that the weight optimization also improves interior quadrature accuracy (cf. Remark 3), the cantilever beam test is repeated on deliberately irregular node distributions. Starting from each uniform grid, all interior node coordinates are randomly perturbed by offsets on the order of 40% of the nominal spacing Δx, while boundary nodes and loading remain unchanged.

Figure 11 shows the four jittered node distributions (left) and the corresponding optimized weights (right). Unlike the uniform case in Figure 10, the weights are no longer nearly constant in the interior; they adapt node-by-node to the

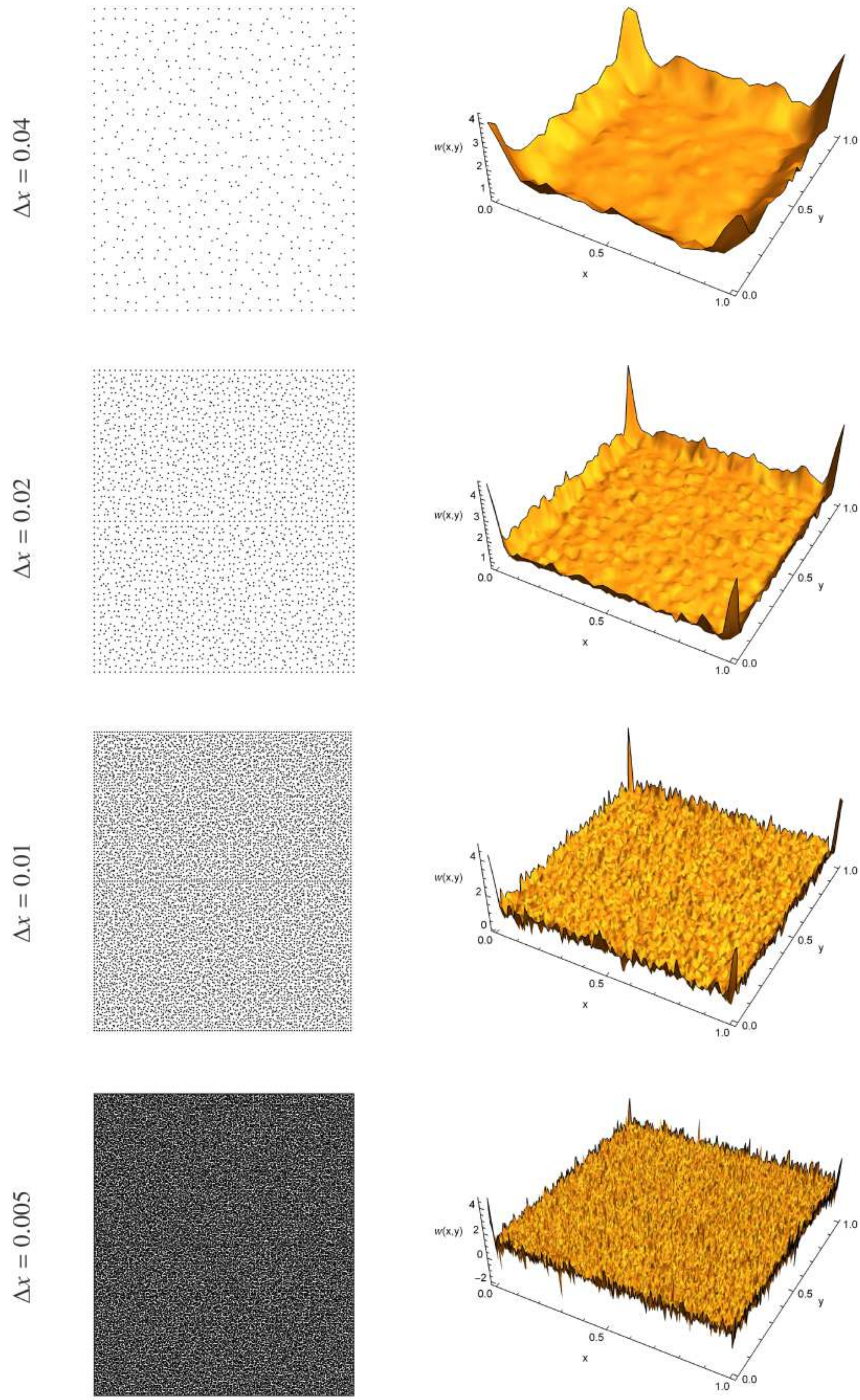

FIGURE 11 | Cantilever beam on irregular node arrangements. Left: jittered node distributions for the four resolutions. Right: optimized nodal influence weights $w(x, y)$ for the same discretizations.

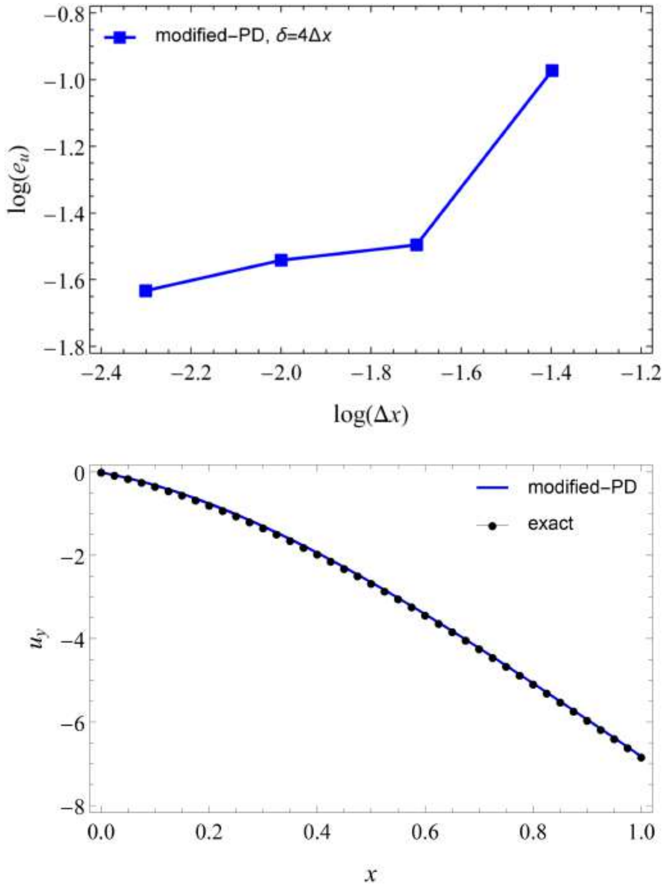

FIGURE 12 | Performance on irregular node distributions (modified-PD only). Top: δ-convergence at fixed $m_{\text{ratio}} = 4$: $\log(e_u)$ versus $\log(\Delta x)$. Bottom: u_y along the midline $y = H/2$ for modified-PD (blue, solid) and the exact solution (73) (black circles) with $\Delta x = 0.01$.

local sampling geometry while still forming a boundary layer of amplified values along free edges. As the discretization is refined, interior fluctuations decrease and the boundary layer narrows, consistent with recovery of the full-horizon energetics.

Figure 12 (top) confirms monotonic error decay under refinement for modified-PD on the irregular grids, consistent with the uniform-grid results in Figure 9 (top). In some cases, the irregular discretization yields slightly lower error than the regular one, because the jitter improves the conditioning of the local moment matrices. Figure 12 (bottom) shows that the modified-PD midline displacement remains in close agreement with the exact solution for $\Delta x = 0.01$.

These results confirm that the proposed optimization provides a robust correction for both boundary and interior nodes, as anticipated in Remark 3. A comparison with PD is omitted for the irregular case, since PD is designed for uniform node distributions and would not constitute a fair baseline.

5.3 | Example 3: Perforated Plate Under Uniaxial Tension

A 2D perforated plate under uniaxial tension is considered to demonstrate the applicability of the proposed approach to curved geometries (see Figure 13). The plate is a square with edge length $2L$ and unit thickness, containing a central circular hole of radius r_0. Exploiting symmetry, only one quarter of the domain is analyzed: the bottom and left edges carry symmetry constraints, while Neumann conditions derived from the exact stress field are applied on the top and right edges.

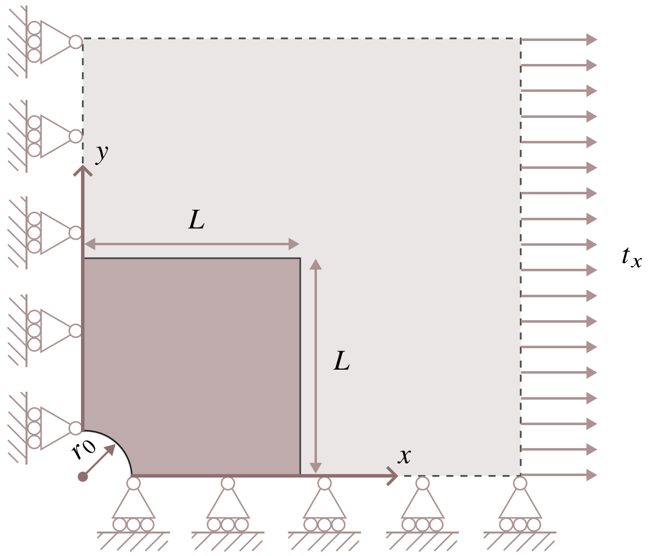

FIGURE 13 | Schematic representation of the problem domain and boundary conditions in Example 3.

The exact CCM reference solution is given by [80]:

$$\sigma_x^{\text{ref}}(r,\theta) = t_x \left[1 - \frac{r_0^2}{r^2}\left(\frac{3}{2}\cos 2\theta + \cos 4\theta\right) + \frac{3r_0^4}{2r^4}\cos 4\theta \right], \tag{74}$$

$$u_r^{\text{ref}}(r,\theta) = \frac{t_x}{4G}\left[r\left(\frac{\kappa-1}{2} + \cos 2\theta\right) + \frac{r_0^2}{r}\left(1 + (1+\kappa)\cos 2\theta - \frac{r_0^4}{r^3}\cos 2\theta\right)\right], \tag{75}$$

$$u_\theta^{\text{ref}}(r,\theta) = \frac{t_x}{4G}\left[(1-\kappa)\frac{r_0^2}{r} - r - \frac{r_0^4}{r^3}\sin 2\theta \right], \tag{76}$$

where (r,θ) are polar coordinates, $G = E/2(1+\nu)$, and $\kappa = (3-\nu)/(1+\nu)$. The parameters are: $L = 4$, $r_0 = 1$, $E = 10$, $\nu = 1/3$ (plane stress), and $t_x = 1$.

A δ-convergence study is performed at fixed $m_{\text{ratio}} = 4$ for $\Delta x \in \{0.1,\ 0.05,\ 0.025,\ 0.0125\}$. Figure 14 (left) shows the node distribution for the representative case $\Delta x = 0.05$, while Figure 14 (right) displays the corresponding optimized weights. Consistent with the cantilever beam results (cf. Figure 10), the weights are nearly constant in the interior and amplified near both flat and curved free edges, forming a boundary layer that compensates for horizon truncation.

Figure 15 reports the convergence results: both modified-PD and PD models exhibit monotonic error decay, with modified-PD yielding consistently lower errors than PD across all resolutions.

5.4 | Example 4: Kalthoff–Winkler Impact (Dynamic Brittle Fracture)

The Kalthoff–Winkler impact experiment [81], a widely used benchmark for dynamic brittle fracture in PD [16, 40, 57, 82–85], is considered (see Figure 16). A rectangular steel 18Ni1900 plate (100×200 mm^2) contains two horizontal, parallel pre-cracks of length 50 mm. A rigid projectile impacts the left edge between the two pre-cracks; experimentally, this triggers Mode I brittle fracture with cracks propagating at approximately 68° from the horizontal [81].

The material parameters are: $E = 190 \times 10^3$ N/mm^2, $\nu = 1/4$ (plane strain), $\rho = 8000 \times 10^{-9}$ kg/mm^3, and $G_0 = 22,170 \times 10^{-6}$ J/mm^2. The impact is modeled by prescribing a constant horizontal velocity $\dot{u}_{x0} = 16.5 \times 10^3$ mm/s to the nodes on the left edge between the pre-cracks. Time integration employs the velocity-Verlet algorithm with $\Delta t = 35$ ns over a total duration of 87.5 μs.

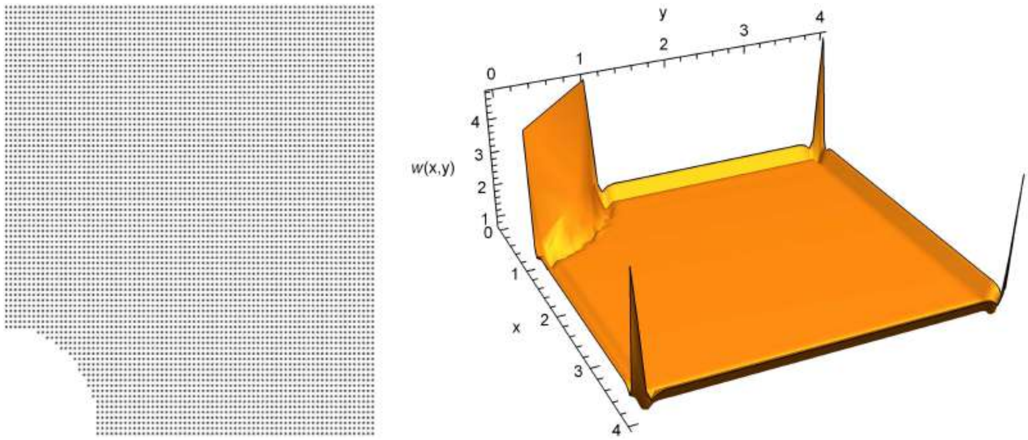

FIGURE 14 | Left: node distribution for the perforated plate with $\Delta x = 0.05$ and $m_{\text{ratio}} = 4$. Right: optimized nodal influence weights $w(x, y)$ for the same discretization.

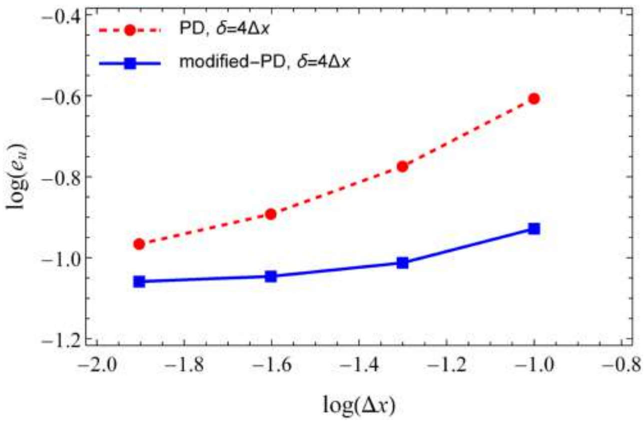

FIGURE 15 | δ-convergence at fixed $m_{\text{ratio}} = 4$: $\log(e_u)$ versus $\log(\Delta x)$ for PD (red, dashed) and modified-PD (blue, solid).

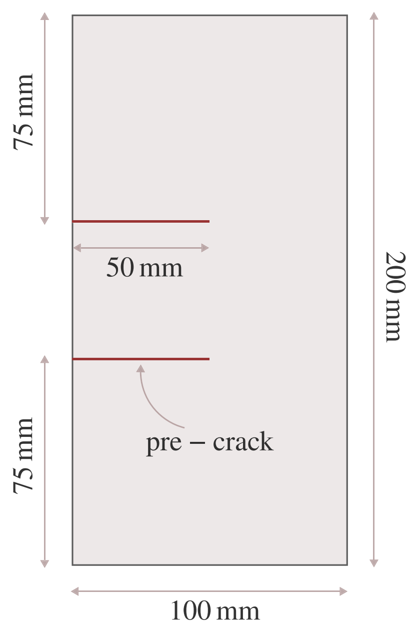

FIGURE 16 | Schematic representation of the problem domain in Example 4.

Standard PD is known to produce spurious boundary-crack nucleation at insufficient spatial resolution; common remedies include local refinement or FEM–PD coupling at increased cost [17, 52]. This example demonstrates that modified-PD suppresses these artifacts at the cost of a coarse simulation. Three models are compared with identical physics and $\delta = 4$ mm: (i) standard PD (coarse), $\Delta x = 0.333$ mm (180 901 nodes); (ii) modified-PD (coarse), same discretization; and (iii) standard PD (fine), $\Delta x = 0.250$ mm (321,201 nodes).

Figure 17 shows the damage evolution at $t \in \{35,\ 52.5,\ 70,\ 87.5\}$ μs. The standard PD (coarse) solution develops unphysical boundary-driven cracks at the right edge around $t \approx 70\ \mu$s, which subsequently interact with the main crack branches.

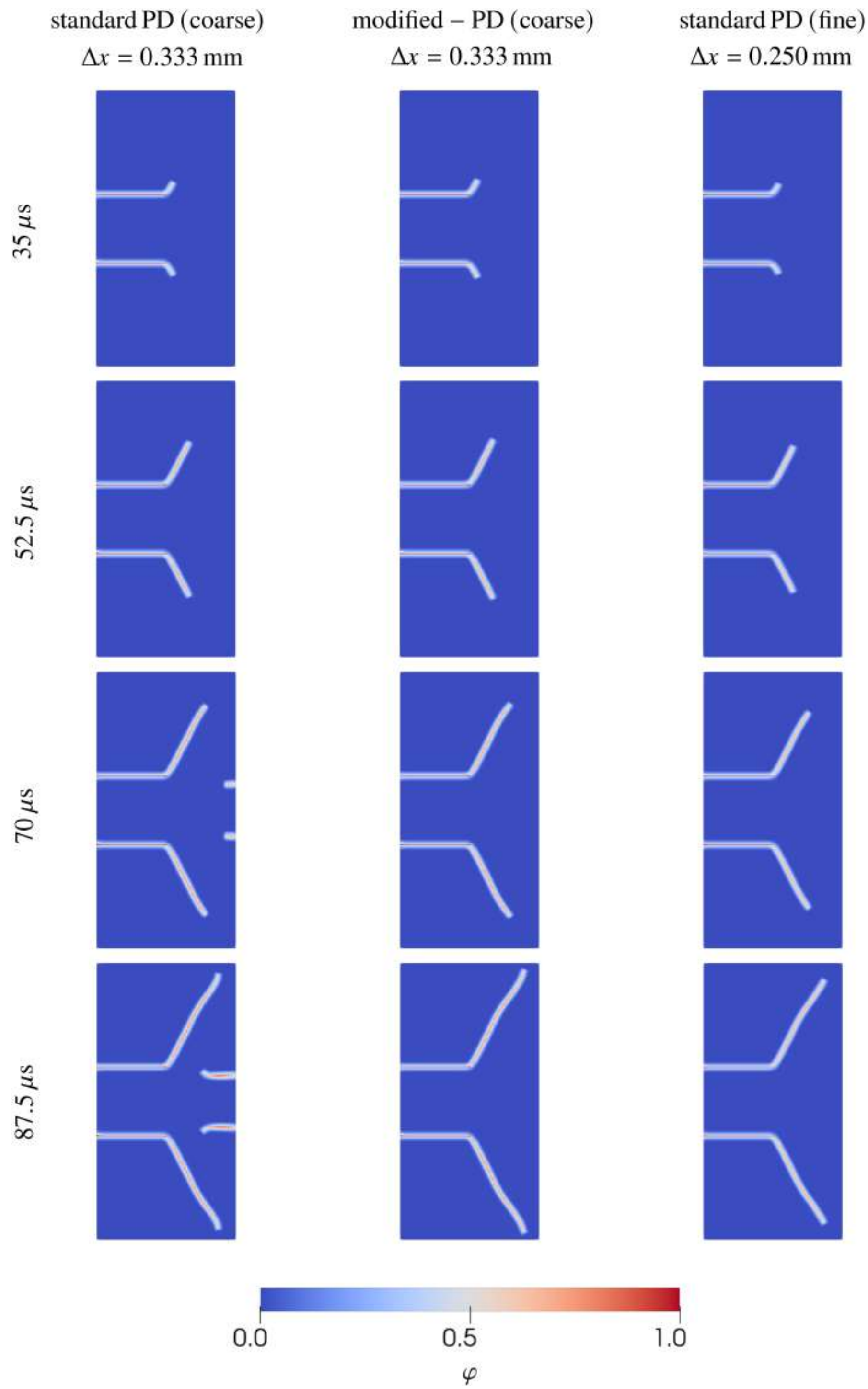

FIGURE 17 | Damage evolution at $t \in \{35,\ 52.5,\ 70,\ 87.5\}$ μs. Columns: standard PD (coarse) ($\Delta x = 0.333$ mm), modified-PD (coarse) ($\Delta x = 0.333$ mm), and standard PD (fine) ($\Delta x = 0.250$ mm), all with $\delta = 4$ mm.

In contrast, modified-PD (coarse) suppresses these artifacts and reproduces crack initiation at the pre-crack tips with propagation closely matching the standard PD (fine) reference. The crack propagation angle, measured from the horizontal pre-crack direction at $t = 87.5$ μs, is approximately 68° for both the modified-PD (coarse) and standard PD (fine) models, in close agreement with the experimentally observed angle of ≈ 68° [81] and consistent with PD results reported in the literature [16, 57, 82].

Figure 18 reports the vertical velocity field $\dot{u}_y$ at the same time instants. The modified-PD fields remain smooth near free boundaries, confirming that the optimized weights alleviate boundary-induced softening without introducing spurious reflections, whereas the standard PD (coarse) results exhibit boundary-driven disturbances consistent with spurious cracking.

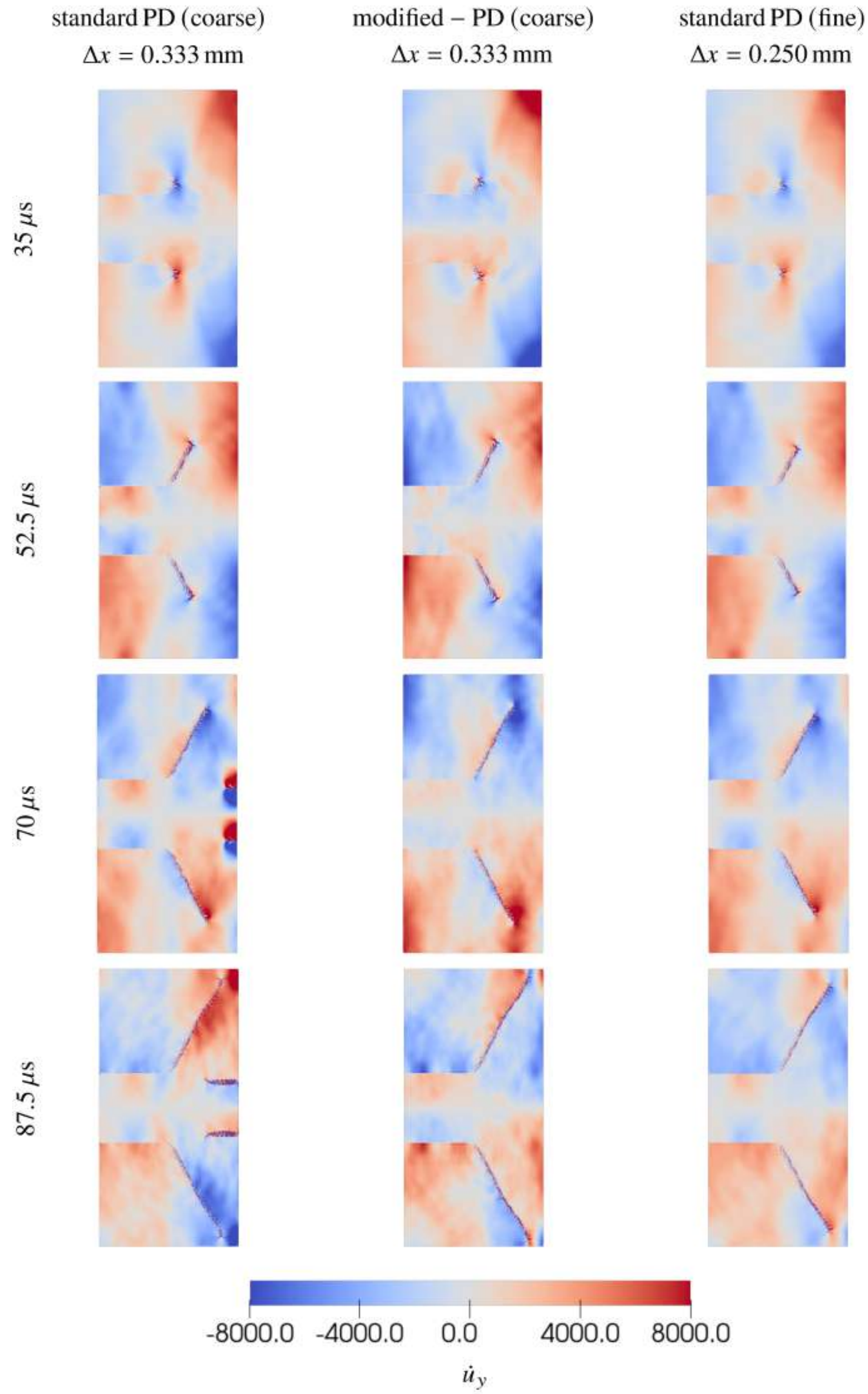

FIGURE 18 | Vertical velocity field $|\dot{u}_y|$ [mm/s] at $t \in \{35,\ 52.5,\ 70,\ 87.5\}$ μs. Columns as in Figure 17.

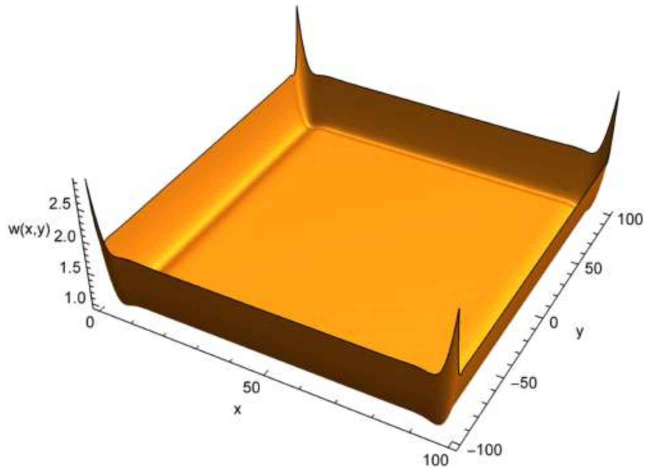

FIGURE 19 | Optimized nodal influence weights $w(x, y)$ for modified-PD (coarse) with $\Delta x = 0.333$ and $\delta = 4$ mm.

Figure 19 displays the weight field $w(x, y)$ for the modified-PD model, exhibiting the characteristic boundary layer of amplified values near free edges and slightly reduced values in the interior.

5.5 | Example 5: Hollow Cylinder Under Torsion

A 3D hollow cylinder under torsion is considered to assess the proposed method on a geometry with curved free surfaces and to compare its performance against the volume correction approach of Le and Bobaru [45], a widely adopted surface-correction strategy in the PD literature. The geometry consists of a hollow cylinder with inner radius $R_1 = 0.5$, outer radius $R_2 = 1$, and length $L = 2$. The material parameters are $E = 1$, $\nu = 1/4$ (plane strain), and $G = E/2(1 + \nu) = 0.4$. A unit torque $T = 1$ is applied at the loaded end $z = L$, while the opposite end $z = 0$ is clamped.

The exact CCM reference solution is the Saint-Venant torsion field:

$$u_x^{\mathrm{ref}} = -\frac{T}{GJ}\, yz, \qquad u_y^{\mathrm{ref}} = +\frac{T}{GJ}\, xz, \qquad u_z^{\mathrm{ref}} = 0, \tag{77}$$

where $J = \pi(R_2^4 - R_1^4)/2$ is the polar moment of inertia. The Dirichlet condition at $z = 0$ and the surface traction at $z = L$ are prescribed from the exact solution; the inner and outer cylindrical surfaces are traction-free.

The volume correction method [45] assigns a per-bond correction factor

$$\lambda_{ij} = \frac{2\, V_0}{V(\mathbf{x}_j) + V(\mathbf{x}_i)}, \tag{78}$$

where $V(\mathbf{x}_i) = \sum_{j \in \mathcal{F}_i} V_j$ is the discrete neighborhood volume of node i, and $V_0 = \frac{4}{3}\pi\delta^3$ is the volume of a full (interior) horizon sphere. Each pairwise bond stiffness is then scaled by λ_{ij}, boosting interactions between nodes whose neighborhoods are truncated by the boundary. This approach partially compensates for the reduced horizon volume near free surfaces but does not enforce operator-level consistency.

A δ-convergence study is performed at fixed $m_{\mathrm{ratio}} \approx 5$ for $\Delta x \in \{0.1,\ 0.0833,\ 0.0714,\ 0.0625\}$, comparing three models: standard PD, volume correction method [45], and modified-PD, for both BB-PD and OSB-PD formulations.

Figure 20 reports the convergence results. Standard PD yields large errors ($e_u \approx 10^{-1}$) with no systematic improvement under refinement, reflecting the persistent surface effect on the curved boundaries. The volume correction method reduces the error by approximately one order of magnitude; however, the error remains nearly flat under refinement, indicating that the correction improves the constant but does not regularize the convergence behavior. In contrast, modified-PD achieves errors two to three orders of magnitude below standard PD and exhibits clear monotonic convergence in both BB-PD and OSB-PD, confirming that the operator-matching calibration produces a systematically improvable discretization.

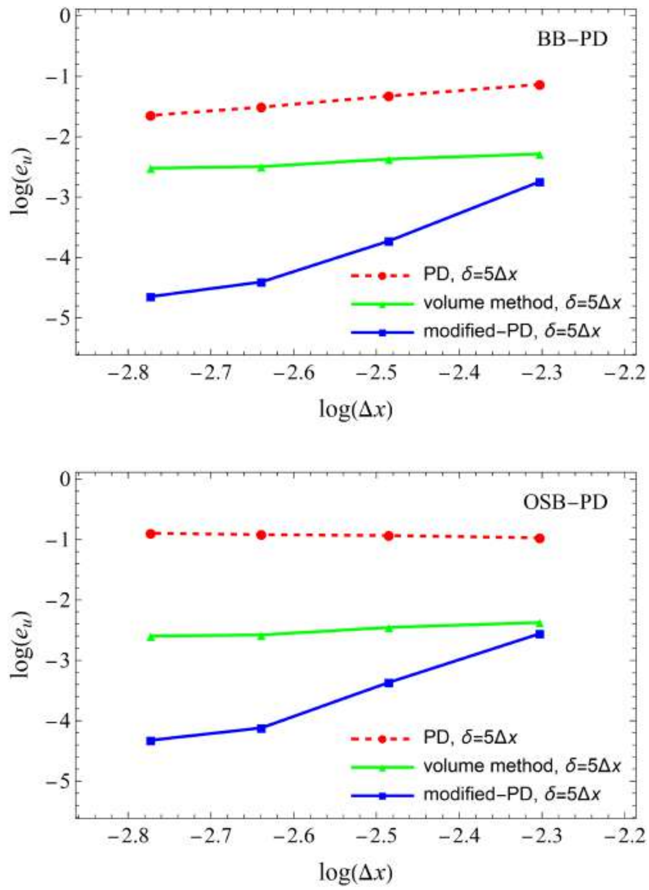

FIGURE 20 | Hollow cylinder under torsion: δ-convergence at fixed $m_{\text{ratio}} \approx 5$: $\log(e_u)$ versus $\log(\Delta x)$ for standard PD (red, dashed), volume correction method [45] (green, solid), and modified-PD (blue, solid) for BB-PD (top) and OSB-PD (bottom).

Figure 21 displays the magnitude of the pointwise displacement error $\|\mathbf{u} - \mathbf{u}^{\text{ref}}\|$ for the finest resolution $\Delta x = 0.0625$. Standard PD concentrates large errors near the inner and outer cylindrical surfaces due to horizon truncation. The volume correction method reduces the surface error substantially but retains a residual pattern, whereas modified-PD yields uniformly low errors throughout the domain for both formulations.

Figure 22 shows the optimized nodal influence weights $w(\mathbf{x})$ at $\Delta x = 0.0625$ for BB-PD and OSB-PD. The weights are amplified near both the inner and outer free surfaces, where the curved geometry causes significant horizon truncation, and approach unity in the bulk interior, consistent with the behavior observed in the 2D examples.

Table 1 reports the computational cost of the weight calibration. The wall time scales approximately linearly with the number of nodes and remains modest (7–33 s for N up to 19,800). The condition number of $\mathbf{K}_w$ grows moderately with refinement and remains below 160 across all resolutions, confirming the well-posedness of the global system (69) on curved 3D geometries.

5.6 | Example 6: Weight Computation on a Complex Geometry

The final example assesses the practical applicability of the proposed weight calibration to an industrially relevant geometry for which no analytical reference solution is available. The objective is not to solve a boundary-value problem, but to verify that the global system (69) can be assembled and solved efficiently on a non-trivial 3D part with mixed flat and curved surfaces, sharp concave corners, and multiple length scales (i.e., δ), and that the resulting weights remain physically reasonable and well-behaved under mesh refinement.

The geometry consists of a crankshaft segment comprising two cylindrical journals connected by two rectangular webs joined at sharp internal corners (Figure 23), spanning approximately $109 \times 100 \times 80$ length units. The domain is

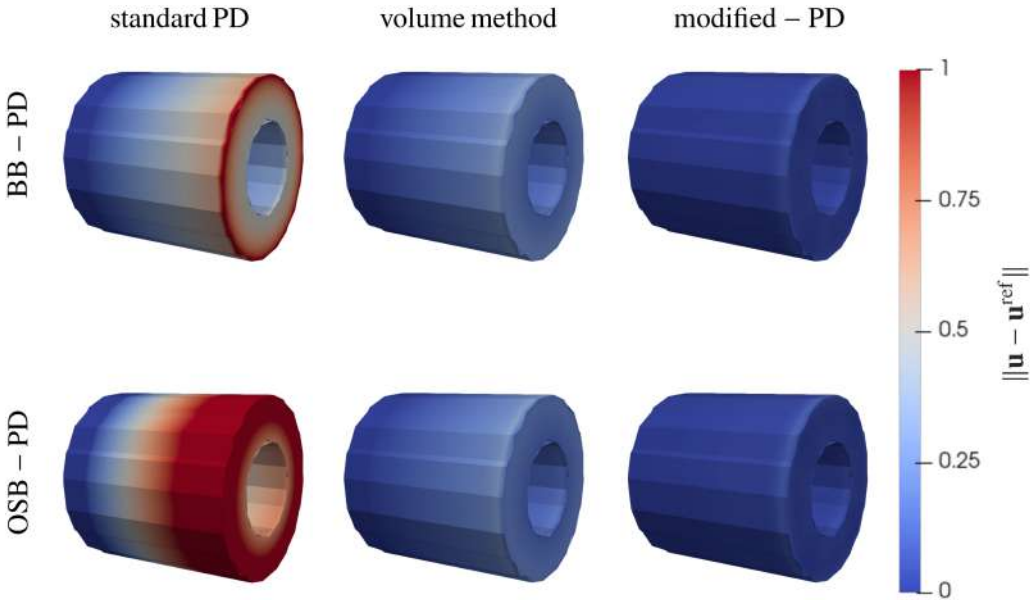

FIGURE 21 | Pointwise displacement error $\|\mathbf{u} - \mathbf{u}^{\mathrm{ref}}\|$ at $\Delta x = 0.0625$ and $m_{\mathrm{ratio}} \approx 5$. Columns: standard PD, volume correction method [45], and modified-PD. Rows: BB-PD (top), and OSB-PD (bottom). The stepped surface pattern reflects the staircase approximation of the curved boundary inherent to the voxelized Cartesian discretization.

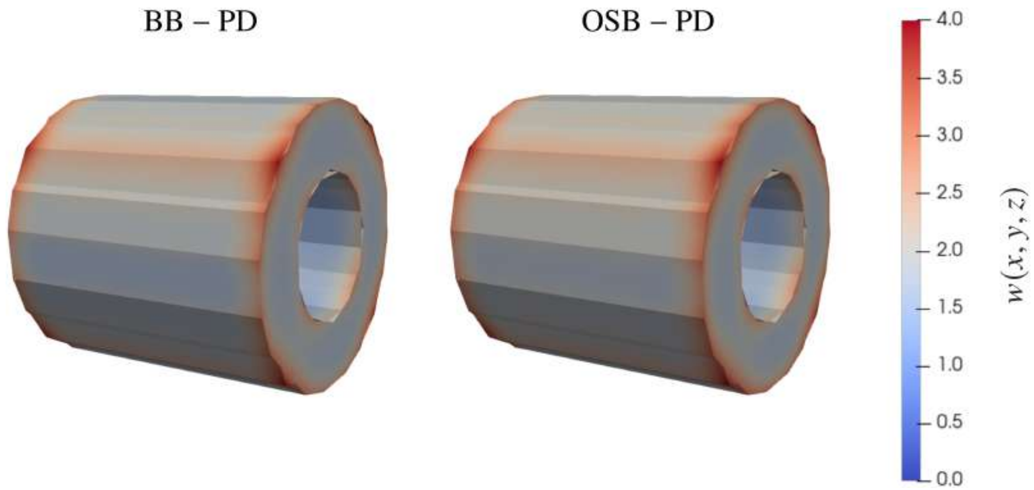

FIGURE 22 | Optimized nodal influence weights $w(\mathbf{x})$ at $\Delta x = 0.0625$ and $m_{\mathrm{ratio}} \approx 5$ for BB-PD (left) and OSB-PD (right). The weights are amplified near the inner and outer cylindrical free surfaces where the neighborhood is truncated.

TABLE 1 | Computational performance of the weight calibration for the hollow cylinder at $m_{\mathrm{ratio}} \approx 5$: wall time (averaged over three runs) measures the assembly and iterative solve of $\mathbf{K}_w\ \mathbf{w} = \mathbf{F}_w$; cond($\mathbf{K}_w$) confirms that the system remains well-conditioned under refinement.

Δx	N	BB-PD [s]	OSB-PD [s]	$\mathrm{cond}_{\mathrm{BB}}$	$\mathrm{cond}_{\mathrm{OSB}}$
0.1000	4956	6.97	6.77	78.6	79.9
0.0833	8200	12.16	12.07	100.2	101.6
0.0714	13,456	21.52	21.36	128.0	129.6
0.0625	19,800	32.90	32.58	154.1	155.9

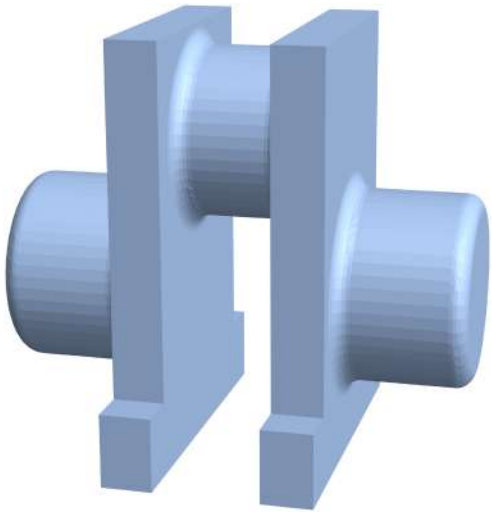

FIGURE 23 | Crankshaft segment geometry used in Example 6. The part combines two cylindrical journals with two rectangular webs joined by sharp internal corners, spanning approximately $109 \times 100 \times 80$ length units.

TABLE 2 | Computational performance of the weight calibration for the crankshaft at $m_{\text{ratio}} = 5$: wall time (averaged over three runs) measures the assembly and iterative solve of the global system $\mathbf{K}_w\ \mathbf{w} = \mathbf{F}_w$, while cond($\mathbf{K}_w$) confirms that the system remains well-conditioned as the discretization is refined.

Δx	N	BB-PD [s]	OSB-PD [s]	cond_{BB}	cond_{OSB}
3.64	7559	11.3	11.5	97.0	98.5
2.44	23,554	40.2	40.2	168.5	170.4
1.82	56,228	101.1	99.0	260.6	263.5
1.43	107,820	202.8	198.5	359.3	362.9

discretized by voxelization from an STL surface mesh at four resolutions, that is, $\Delta x \in \{3.64,\ 2.44,\ 1.82,\ 1.43\}$, with fixed $m_{\text{ratio}} = 5$, yielding N from 7559 to 107,820 nodes.

Table 2 reports the computational cost and condition number of $\mathbf{K}_w$ for both BB-PD and OSB-PD. The wall time scales approximately linearly with N and remains practical even at the finest resolution (approximately 200 s for $N \approx 108,000$ nodes on a single CPU core). The condition number grows moderately with refinement, reaching cond($\mathbf{K}_w$) ≈ 360 at the finest mesh, well within the range of standard iterative solvers and comparable in magnitude to the hollow cylinder in Example 5, despite the significantly more complex geometry. The near-identical timings and condition numbers for BB-PD and OSB-PD confirm that both formulations lead to systems of comparable difficulty on the same point set.

A δ-convergence study of the weight field is performed at fixed $m_{\text{ratio}} = 5$. As the mesh is refined, the median weight converges toward unity, confirming that the majority of interior nodes require negligible correction. The maximum weight stabilizes around 4–5, corresponding to nodes at the most severely truncated locations (sharp concave corners and cylinder ends), while the minimum remains above 0.6, indicating that no node is excessively attenuated. At the finest resolution ($\Delta x = 1.43$), the BB-PD weights lie in the range $[0.69,\ 4.47]$ with a median of 1.07; the OSB-PD weights span $[0.66,\ 4.62]$ with a median of 1.08. The 5th–95th percentile band ($[0.91,\ 2.16]$ for BB-PD) narrows with refinement, reflecting the decreasing fraction of nodes whose horizons are affected by boundary truncation.

Figure 24 displays the spatial distribution of the optimized weights at $\Delta x = 1.43$ for BB-PD and OSB-PD. The weight contours exhibit the same qualitative behavior observed in the preceding examples: values close to unity in the bulk interior and amplified at free surfaces and internal concavities where the horizon is truncated. The highest weights ($w \approx$ 3–4) occur at the sharp internal corners between webs and journals and along the cylindrical free surfaces, consistent with the physical expectation that these regions suffer the most severe horizon loss. The BB-PD and OSB-PD weight distributions are nearly indistinguishable, consistent with the observation that the two formulations differ only through the kernel exponent q in (54).

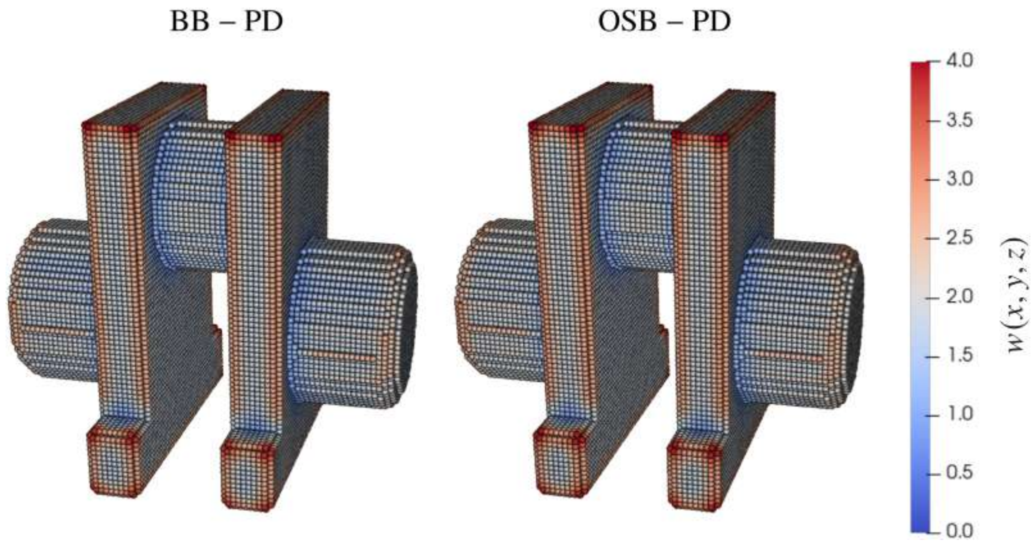

FIGURE 24 | Optimized nodal influence weights $w(\mathbf{x})$ at $\Delta x = 1.43$ and $m_{\text{ratio}} = 5$ for BB-PD (left) and OSB-PD (right). Weights are amplified near cylindrical free surfaces and sharp internal corners where horizon truncation is most pronounced, and approach unity in the bulk interior.

Overall, this example demonstrates that the proposed weight calibration scales to geometrically complex 3D parts with $O(10^5)$ nodes at acceptable cost, produces physically meaningful and bounded weight fields, and yields a well-conditioned global system regardless of the geometric complexity. The resulting weights can be employed in any subsequent BB-PD or OSB-PD simulation formulated on the same point set and horizon without recomputation.

6 | Conclusions

This work addresses the surface effect in peridynamics (PD) caused by horizon truncation near domain boundaries, which induces operator-level inconsistencies manifesting as artificial softening in BB PD and relative stiffening in OSB PD. A modal analysis traces both defects to a common algebraic origin: the activation of odd horizon moments on asymmetric integration domains.

A purely PD-based correction is proposed, in which each node receives a scalar influence weight and every bond is scaled symmetrically by the average of the endpoint weights. This construction preserves pairwise reciprocity and global stiffness symmetry without introducing fictitious nodes, variable horizons, or reference solutions from CCM. The weights are determined once in a load-independent preprocessing step by matching truncated-horizon derivative and energy operators against their analytical full-horizon counterparts on a local polynomial test space. The same formulation applies to both BB-PD and OSB-PD, differing only through the kernel exponent of the respective operators.

Numerical examples in one, two, and three dimensions confirm the effectiveness of the approach. In static problems with exact solutions, modified-PD yields errors consistently lower than standard PD, by up to two to three orders of magnitude in the 3D case, and exhibits regular monotonic δ-convergence on both uniform and irregular node distributions, on flat and curved boundaries alike. The comparison with a widely used volume correction method for the 3D hollow cylinder shows that, while volume correction reduces the error, it does not regularize the convergence behavior; modified-PD achieves both. In dynamic brittle fracture, the optimized weights suppress spurious boundary-driven cracks at coarse resolution while preserving physically meaningful crack paths. On a geometrically complex industrial part with $O(10^5)$ nodes, the calibration remains practical (minutes on a single core) and the global system stays well-conditioned, demonstrating scalability to real-world geometries.

The proposed strategy offers a simple and portable remedy for boundary-induced artifacts at essentially the cost of a single sparse linear solve. Since the analytical full-horizon targets are geometry-dependent but load-independent, the same weights can be reused across different boundary-value problems on the same point set and horizon. The procedure integrates seamlessly into existing PD codes and is available as the open-source Python package `perifit`.

Author Contributions

Arman Shojaei: conceptualization, formal analysis, investigation, methodology, software, validation, writing – original draft, writing – review and editing. **Greta Ongaro:** formal analysis, investigation, visualization, writing – original draft, writing – review and editing. **Alexander Hermann:** formal analysis, investigation, software, validation, writing – original draft. **Stewart A. Silling:** validation, investigation, supervision, writing – review and editing. **Patrizia Trovalusci:** funding acquisition, resources, supervision, writing – review and editing. **Christian J. Cyron:** funding acquisition, resources, supervision, writing – review and editing.

Acknowledgments

Funded by the Deutsche Forschungsgemeinschaft (DFG, German Research Foundation) under Germany's Excellence Strategy – EXC 3120/1 – 533771286. This work was supported by the IDIR-Project (Digital Implant Research), a cooperation financed by Kiel University, University Hospital Schleswig-Holstein and Helmholtz Zentrum Hereon. This work was supported by MIUR, project: National Center on HPC, Big Data and Quantum Computing (ICSC), PNRR - CN1- Spoke6 (CUP: B83C22002940006), and PROGETTO MUSICS - FISA-2023-00099 (CUP: B83C25000810001). Open Access funding enabled and organized by Projekt DEAL.

Funding

This work was supported by the Deutsche Forschungsgemeinschaft (DFG) (Grant No. EXC 3120/1 – 533771286) and the Ministero dell'Istruzione, dell'Università e della Ricerca (Grant Nos. CUP: B83C22002940006 and CUP: B83C25000810001).

Conflicts of Interest

The authors declare no conflicts of interest.

Data Availability Statement

Data sharing not applicable to this article as no datasets were generated or analyzed during the current study.

References

1. S. A. Silling, "Reformulation of Elasticity Theory for Discontinuities and Long-Range Forces," *Journal of the Mechanics and Physics of Solids* 48, no. 1 (2000): 175–209.

2. S. A. Silling, M. Epton, O. Weckner, J. Xu, and E. Askari, "Peridynamic States and Constitutive Modeling," *Journal of Elasticity* 88, no. 2 (2007): 151–184.

3. S. A. Silling, "Linearized Theory of Peridynamic States," *Journal of Elasticity* 99, no. 1 (2010): 85–111.

4. F. Bobaru and W. Hu, "The Meaning, Selection, and Use of the Peridynamic Horizon and Its Relation to Crack Branching in Brittle Materials," *International Journal of Fracture* 176, no. 2 (2012): 215–222.

5. G. Ongaro, P. Seleson, U. Galvanetto, T. Ni, and M. Zaccariotto, "Overall Equilibrium in the Coupling of Peridynamics and Classical Continuum Mechanics," *Computer Methods in Applied Mechanics and Engineering* 381 (2021): 113515.

6. W.-J. Li, T. You, T. Ni, Q.-Z. Zhu, and L. Hien Poh, "The Extended Peridynamic Model for Elastoplastic and/or Fracture Problems," *International Journal for Numerical Methods in Engineering* 123, no. 21 (2022): 5201–5229.

7. Q.-z. Zhu and T. Ni, "Peridynamic Formulations Enriched With Bond Rotation Effects," *International Journal of Engineering Science* 121 (2017): 118–129.

8. Y. Wang, X. Zhou, Y. Wang, and Y. Shou, "A 3-D Conjugated Bond-Pair-Based Peridynamic Formulation for Initiation and Propagation of Cracks in Brittle Solids," *International Journal of Solids and Structures* 134 (2018): 89–115.

9. V. Diana and S. Casolo, "A Bond-Based Micropolar Peridynamic Model With Shear Deformability: Elasticity, Failure Properties and Initial Yield Domains," *International Journal of Solids and Structures* 160 (2019): 201–231.

10. H. Yu, X. Chen, and Y. Sun, "A Generalized Bond-Based Peridynamic Model for Quasi-Brittle Materials Enriched With Bond Tension–Rotation–Shear Coupling Effects," *Computer Methods in Applied Mechanics and Engineering* 372 (2020): 113405.

11. Y.-T. Wang, X.-P. Zhou, and M.-M. Kou, "Three-Dimensional Numerical Study on the Failure Characteristics of Intermittent Fissures Under Compressive-Shear Loads," *Acta Geotechnica* 14, no. 4 (2019): 1161–1193.

12. S. A. Silling and E. Askari, "A Meshfree Method Based on the Peridynamic Model of Solid Mechanics," *Computers & Structures* 83, no. 17–18 (2005): 1526–1535.

13. J. Xu, A. Askari, O. Weckner, and S. Silling, "Peridynamic Analysis of Impact Damage in Composite Laminates," *Journal of Aerospace Engineering* 21, no. 3 (2008): 187–194.

14. S. Silling, "Dynamic Fracture Modeling With a Meshfree Peridynamic Code," in *Computational Fluid and Solid Mechanics 2003* (Elsevier, 2003), 641–644.

15. A. Shojaei, T. Mudric, M. Zaccariotto, and U. Galvanetto, "A Coupled Meshless Finite Point/Peridynamic Method for 2D Dynamic Fracture Analysis," *International Journal of Mechanical Sciences* 119 (2016): 419–431.

16. A. Shojaei, F. Mossaiby, M. Zaccariotto, and U. Galvanetto, "An Adaptive Multi-Grid Peridynamic Method for Dynamic Fracture Analysis," *International Journal of Mechanical Sciences* 144 (2018): 600–617.

17. F. Mossaiby, P. Sheikhbahaei, and A. Shojaei, "Multi-Adaptive Coupling of Finite Element Meshes With Peridynamic Grids: Robust Implementation and Potential Applications," *Engineering With Computers* 39, no. 4 (2023): 2807–2828.

18. J. Li, S. Liu, F. Han, Y. Mei, Y. Sun, and F. Zhou, "Adaptive Coupling of Peridynamic and Classical Continuum Mechanical Models Driven by Broken Bond/Strength Criteria for Structural Dynamic Failure," *International Journal for Numerical Methods in Engineering* 126, no. 7 (2025): e70021.

19. Y. Yu, F. Han, Z. Li, Y. Sun, Y. Mei, and A. Zhang, "Element-Based Coupling Modeling of Peridynamics and Classical Continuum Mechanics for Dynamic Brittle Fracture," *International Journal for Numerical Methods in Engineering* 124, no. 24 (2023): 5574–5595.

20. Y. Hu and E. Madenci, "Peridynamics for Fatigue Life and Residual Strength Prediction of Composite Laminates," *Composite Structures* 160 (2017): 169–184.

21. F. Bobaru and M. Duangpanya, "The Peridynamic Formulation for Transient Heat Conduction," *International Journal of Heat and Mass Transfer* 53, no. 19–20 (2010): 4047–4059.

22. A. Shojaei, A. Hermann, P. Seleson, and C. J. Cyron, "Dirichlet Absorbing Boundary Conditions for Classical and Peridynamic Diffusion-Type Models," *Computational Mechanics* 66, no. 4 (2020): 773–793.

23. Z. Chen and F. Bobaru, "Peridynamic Modeling of Pitting Corrosion Damage," *Journal of the Mechanics and Physics of Solids* 78 (2015): 352–381.

24. A. Hermann, A. Shojaei, D. Steglich, D. Höche, B. Zeller-Plumhoff, and C. J. Cyron, "Combining Peridynamic and Finite Element Simulations to Capture the Corrosion of Degradable Bone Implants and to Predict Their Residual Strength," *International Journal of Mechanical Sciences* 220 (2022): 107143.

25. C. J. Cyron, M. Fritz, A. Hermann, T. Köppl, A. Shojaei, and S. A. Silling, "Unifying Local and Nonlocal Corrosion Frameworks: A Convergent Nonlocal Extension of the KKS Phase-Field Model," 2025, https://doi.org/10.48550/arXiv.2509.23503.

26. Y. Du and J. Zhang, "Perfectly Matched Layers for Peridynamic Scalar Waves and the Numerical Discretization on Real Coordinate Space," *International Journal for Numerical Methods in Engineering* 125, no. 3 (2024): e7392.

27. W. Gerstle, N. Sau, and S. Silling, "Peridynamic Modeling of Concrete Structures," *Nuclear Engineering and Design* 237, no. 12–13 (2007): 1250–1258.

28. E. Oterkus and E. Madenci, "Peridynamic Analysis of Fiber-Reinforced Composite Materials," *Journal of Mechanics of Materials and Structures* 7, no. 1 (2012): 45–84.

29. V. A. Buryachenko, "Peridynamic Micromechanics of Composites: A Review," *Journal of Peridynamics and Nonlocal Modeling* 6, no. 4 (2024): 531–601.

30. F. Scabbia, V. Diana, F. Fantoni, M. Zaccariotto, and U. Galvanetto, "Peridynamic Correspondence Model for Nearly-Incompressible Finite Elasticity," *Computer Methods in Applied Mechanics and Engineering* 447 (2025): 118350.

31. J. Guan, W. Li, X. Yan, and L. Guo, "An Incremental Bond-Based Peridynamic Method for Elastoplastic Problems," *International Journal for Numerical Methods in Engineering* 124, no. 17 (2023): 3875–3902.

32. J. Wang, M. Behzadinasab, W. Li, and Y. Bazilevs, "A Stable Formulation of Correspondence-Based Peridynamics With a Computational Structure of a Method Using Nodal Integration," *International Journal for Numerical Methods in Engineering* 125, no. 11 (2024): e7465.

33. S. Jafarzadeh, Z. Chen, S. Li, and F. Bobaru, "A Peridynamic Mechano-Chemical Damage Model for Stress-Assisted Corrosion," *Electrochimica Acta* 323 (2019): 134795.

34. V. Diana and V. Carvelli, "An Electromechanical Micropolar Peridynamic Model," *Computer Methods in Applied Mechanics and Engineering* 365 (2020): 112998.

35. S. Bazazzadeh, M. Morandini, M. Zaccariotto, and U. Galvanetto, "Simulation of Chemo-Thermo-Mechanical Problems in Cement-Based Materials With Peridynamics," *Meccanica* 56, no. 9 (2021): 2357–2379.

36. J. Fan and H. Xie, "Peridynamic Thermal Stresses and Hypothetical Body Forces," *International Journal for Numerical Methods in Engineering* 126, no. 21 (2025): e70154.

37. S. Bazazzadeh, F. Mossaiby, and A. Shojaei, "An Adaptive Thermo-Mechanical Peridynamic Model for Fracture Analysis in Ceramics," *Engineering Fracture Mechanics* 223 (2020): 106708.

38. T. Ni, J. Zhang, M. Zaccariotto, U. Galvanetto, and B. A. Schrefler, "Matrix-Based Implementation and GPU Acceleration of Hybrid FEM and Peridynamic Model for Hydro-Mechanical Coupled Problems," *International Journal for Numerical Methods in Engineering* 125, no. 18 (2024): e7504.

39. F. Scabbia and M. Enea, "An Improved Coupling of 3D State-Based Peridynamics With High-Order 1D Finite Elements to Reduce Spurious Effects at Interfaces," *International Journal for Numerical Methods in Engineering* 124, no. 17 (2023): 3687–3708.

40. M. Zaccariotto, T. Mudric, D. Tomasi, A. Shojaei, and U. Galvanetto, "Coupling of FEM Meshes With Peridynamic Grids," *Computer Methods in Applied Mechanics and Engineering* 330 (2018): 471–497.

41. R. W. Macek and S. A. Silling, "Peridynamics via Finite Element Analysis," *Finite Elements in Analysis and Design* 43, no. 15 (2007): 1169–1178.

42. B. Aksoylu and M. L. Parks, "Variational Theory and Domain Decomposition for Nonlocal Problems," *Applied Mathematics and Computation* 217, no. 14 (2011): 6498–6515.

43. Q. Du, M. Gunzburger, R. B. Lehoucq, and K. Zhou, "A Nonlocal Vector Calculus, Nonlocal Volume-Constrained Problems, and Nonlocal Balance Laws," *Mathematical Models and Methods in Applied Sciences* 23, no. 3 (2013): 493–540.

44. F. Scabbia, M. Zaccariotto, and U. Galvanetto, "A New Surface Node Method to Accurately Model the Mechanical Behavior of the Boundary in 3D State-Based Peridynamics," *Journal of Peridynamics and Nonlocal Modeling* 5, no. 4 (2023): 521–555.

45. Q. Le and F. Bobaru, "Surface Corrections for Peridynamic Models in Elasticity and Fracture," *Computational Mechanics* 61, no. 4 (2018): 499–518.

46. F. Scabbia, M. Zaccariotto, and U. Galvanetto, "A New Method Based on Taylor Expansion and Nearest-Node Strategy to Impose Dirichlet and Neumann Boundary Conditions in Ordinary State-Based Peridynamics," *Computational Mechanics* 70 (2022): 1–27.

47. M. L. Parks, R. B. Lehoucq, S. J. Plimpton, and S. A. Silling, "Implementing Peridynamics Within a Molecular Dynamics Code," *Computer Physics Communications* 179, no. 11 (2008): 777–783.

48. E. Madenci and E. Oterkus, *Peridynamic Theory and Its Applications* (Springer, 2014), https://doi.org/10.1007/978-1-4614-8465-3.

49. S. Prudhomme and P. Diehl, "On the Treatment of Boundary Conditions for Bond-Based Peridynamic Models," *Computer Methods in Applied Mechanics and Engineering* 372 (2020): 113391.

50. J. Ritter, S. Shegufta, P. Steinmann, and M. Zaiser, "An Energetically Consistent Surface Correction Method for Bond-Based Peridynamics," *Forces in Mechanics* 9 (2022): 100132.

51. S. Shen, Z. Yang, F. Han, J. Cui, and J. Zhang, "Peridynamic Modeling With Energy-Based Surface Correction for Fracture Simulation of Random Porous Materials," *Theoretical and Applied Fracture Mechanics* 114 (2021): 102987.

52. G. Ongaro, A. Shojaei, F. Mossaiby, A. Hermann, C. J. Cyron, and P. Trovalusci, "Multi-Adaptive Spatial Discretization of Bond-Based Peridynamics," *International Journal of Fracture* 244, no. 1 (2023): 1–24.

53. J. Bartlett and D. Storti, "A Generalized Fictitious Node Approach for Surface Effect Correction in Peridynamic Simulation," *Journal of Peridynamics and Nonlocal Modeling* 3, no. 3 (2021): 276–286.

54. Z. Dai, J. Xie, Z. Lu, S. Qin, and L. Wang, "Numerical Modeling on Crack Propagation Based on a Multi-Grid Bond-Based Dual-Horizon Peridynamics," *Mathematics* 9, no. 22 (2021): 2848.

55. S. Shangkun, Y. Zihao, C. Junzhi, and Z. Jieqiong, "Dual-Variable-Horizon Peridynamics and Continuum Mechanics Coupling Modeling and Adaptive Fracture Simulation in Porous Materials," *Engineering With Computers* 39, no. 5 (2023): 3207–3227.

56. H. Ren, X. Zhuang, Y. Cai, and T. Rabczuk, "Dual-Horizon Peridynamics," *International Journal for Numerical Methods in Engineering* 108, no. 12 (2016): 1451–1476.

57. D. Dipasquale, M. Zaccariotto, and U. Galvanetto, "Crack Propagation With Adaptive Grid Refinement in 2D Peridynamics," *International Journal of Fracture* 190, no. 1 (2014): 1–22.

58. B. Kilic and E. Madenci, "Coupling of Peridynamic Theory and the Finite Element Method," *Journal of Mechanics of Materials and Structures* 5, no. 5 (2010): 707–733.

59. P. Seleson, S. Beneddine, and S. Prudhomme, "A Force-Based Coupling Scheme for Peridynamics and Classical Elasticity," *Computational Materials Science* 66 (2013): 34–49.

60. F. Han, G. Lubineau, Y. Azdoud, and A. Askari, "A Morphing Approach to Couple State-Based Peridynamics With Classical Continuum Mechanics," *Computer Methods in Applied Mechanics and Engineering* 301 (2016): 336–358.

61. U. Galvanetto, T. Mudric, A. Shojaei, and M. Zaccariotto, "An Effective Way to Couple Fem Meshes and Peridynamics Grids for the Solution of Static Equilibrium Problems," *Mechanics Research Communications* 76 (2016): 41–47.

62. M. Tuna, G. Ongaro, P. Trovalusci, et al., "Computational Approaches for Crack Propagation in Materials and Structures: Comparison Between Linear Elastic Fracture Mechanics (LEFM) and Peridynamics (PD) Based Strategies," in *Comprehensive Mechanics of Materials* (Elsevier, 2024), 87–103.

63. A. Hermann and A. Shojaei, "Perifit: Perifit v2.0.1," 2026, https://doi.org/10.5281/zenodo.20323593.

64. P. Seleson and D. J. Littlewood, "Convergence Studies in Meshfree Peridynamic Simulations," *Computers & Mathematics With Applications* 71, no. 11 (2016): 2432–2448.

65. P. Seleson and M. Parks, "On the Role of the Influence Function in the Peridynamic Theory," *International Journal for Multiscale Computational Engineering* 9, no. 6 (2011): 689–706, https://doi.org/10.1615/IntJMultCompEng.201100252.

66. F. Bobaru, M. Yang, L. F. Alves, S. A. Silling, E. Askari, and J. Xu, "Convergence, Adaptive Refinement, and Scaling in 1D Peridynamics," *International Journal for Numerical Methods in Engineering* 77, no. 6 (2009): 852–877.

67. J. Trageser and P. Seleson, "Bond-Based Peridynamics: A Tale of Two Poisson's Ratios," *Journal of Peridynamics and Nonlocal Modeling* 2, no. 3 (2020): 278–288.

68. P. Seleson, Y. D. Ha, and S. Beneddine, "Concurrent Coupling of Bond-Based Peridynamics and the Navier Equation of Classical Elasticity by Blending," *International Journal for Multiscale Computational Engineering* 13, no. 2 (2015): 91–113, https://doi.org/10.1615/IntJMultCompEng.2014011338.

69. A. Shojaei, A. Hermann, C. J. Cyron, P. Seleson, and S. A. Silling, "A Hybrid Meshfree Discretization to Improve the Numerical Performance of Peridynamic Models," *Computer Methods in Applied Mechanics and Engineering* 391 (2022): 114544.

70. K. Yu, X. Xin, and K. Lease, "A New Adaptive Integration Method for the Peridynamic Theory," *Modelling and Simulation in Materials Science and Engineering* 19, no. 4 (2011): 045003.

71. F. Mossaiby, G. Häfner, A. Shojaei, et al., "On Efficient Simulation of Self-Assembling Diblock Copolymers Using a Peridynamic-Enhanced Fourier Spectral Method," *Computer Methods in Applied Mechanics and Engineering* 439 (2025): 117878.

72. A. Shojaei, F. Mossaiby, M. Zaccariotto, and U. Galvanetto, "A Local Collocation Method to Construct Dirichlet-Type Absorbing Boundary Conditions for Transient Scalar Wave Propagation Problems," *Computer Methods in Applied Mechanics and Engineering* 356 (2019): 629–651.

73. F. Mossaiby, A. Shojaei, B. Boroomand, M. Zaccariotto, and U. Galvanetto, "Local Dirichlet-Type Absorbing Boundary Conditions for Transient Elastic Wave Propagation Problems," *Computer Methods in Applied Mechanics and Engineering* 362 (2020): 112856.

74. A. Shojaei, A. Hermann, P. Seleson, S. A. Silling, T. Rabczuk, and C. J. Cyron, "Peridynamic Elastic Waves in Two-Dimensional Unbounded Domains: Construction of Nonlocal Dirichlet-Type Absorbing Boundary Conditions," *Computer Methods in Applied Mechanics and Engineering* 407 (2023): 115948.

75. A. Shojaei, U. Galvanetto, T. Rabczuk, A. Jenabi, and M. Zaccariotto, "A Generalized Finite Difference Method Based on the Peridynamic Differential Operator for the Solution of Problems in Bounded and Unbounded Domains," *Computer Methods in Applied Mechanics and Engineering* 343 (2019): 100–126.

76. A. Hermann, A. Shojaei, P. Seleson, C. J. Cyron, and S. A. Silling, "Dirichlet-Type Absorbing Boundary Conditions for Peridynamic Scalar Waves in Two-Dimensional Viscous Media," *International Journal for Numerical Methods in Engineering* 124, no. 16 (2023): 3524–3553.

77. M. Pasetto, Y. Leng, J.-S. Chen, J. T. Foster, and P. Seleson, "A Reproducing Kernel Enhanced Approach for Peridynamic Solutions," *Computer Methods in Applied Mechanics and Engineering* 340 (2018): 1044–1078.

78. N. Trask, H. You, Y. Yu, and M. L. Parks, "An Asymptotically Compatible Meshfree Quadrature Rule for Nonlocal Problems With Applications to Peridynamics," *Computer Methods in Applied Mechanics and Engineering* 343 (2019): 151–165.

79. M. Sotudeh, F. Mossaiby, and A. Shojaei, "On Efficient Numerical Integration for Peridynamic Modeling," *Computational Mechanics* 76 (2025): 1659–1687, https://doi.org/10.1007/s00466-025-02667-5.

80. A. Shojaei, B. Boroomand, and F. Mossaiby, "A Simple Meshless Method for Challenging Engineering Problems," *Engineering Computations* 32, no. 6 (2015): 1567–1600.

81. J. F. Kalthoff, "Modes of Dynamic Shear Failure in Solids," *International Journal of Fracture* 101, no. 1 (2000): 1–31.

82. H. Ren, X. Zhuang, and T. Rabczuk, "Dual-Horizon Peridynamics: A Stable Solution to Varying Horizons," *Computer Methods in Applied Mechanics and Engineering* 318 (2017): 762–782.

83. H. Ren, X. Zhuang, C. Anitescu, and T. Rabczuk, "An Explicit Phase Field Method for Brittle Dynamic Fracture," *Computers & Structures* 217 (2019): 45–56.

84. Y. Ning, X. Liu, G. Kang, and Q. Lu, "Simulations of Crack Development in Brittle Materials Under Dynamic Loading Using the Numerical Manifold Method," *Engineering Fracture Mechanics* 275 (2022): 108830.

85. M. Sotudeh, F. Mossaiby, and A. Shojaei, "Hybrid Meshfree Discretization of Peridynamics: CPU–GPU Performance Comparison," *Journal of Peridynamics and Nonlocal Modeling* 7, no. 4 (2025): 12.